

2 Spacecraft Thermal Environments

J. F. Clawson,^{*} G. T. Tsuyuki,^{*} B. J. Anderson,[†] C. G. Justus,[‡]
W. Batts,[‡] D. Ferguson,^{**} and D. G. Gilmore^{††}

Environments of Earth Orbit

Spacecraft thermal control is a process of energy management in which environmental heating plays a major role. The principal forms of environmental heating on orbit are direct sunlight, sunlight reflected off Earth (albedo), and infrared (IR) energy emitted from Earth. During launch or in exceptionally low orbits, there is also a free molecular heating effect caused by friction in the rarefied upper atmosphere. This chapter gives an overview of these types of environmental heating.

The overall thermal control of a satellite on orbit is usually achieved by balancing the energy emitted by the spacecraft as IR radiation against the energy dissipated by its internal electrical components plus the energy absorbed from the environment; atmospheric convection is absent in space. Figure 2.1 illustrates this relationship.

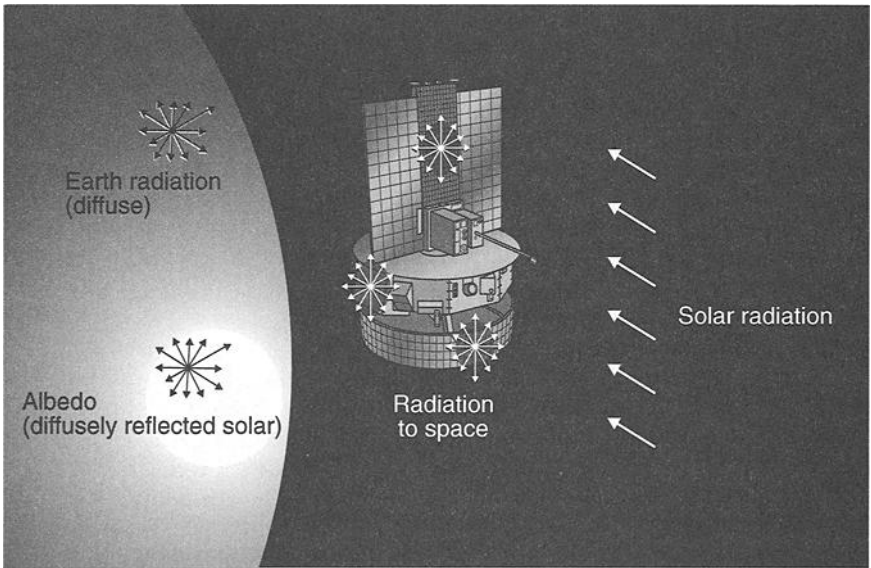


Fig. 2.1. Satellite thermal environment.

^{*}Jet Propulsion Laboratory, California Institute of Technology, Pasadena, California.

[†]NASA/MSFC, Huntsville, Alabama.

[‡]Computer Sciences Corporation, Huntsville, Alabama.

^{**}Swales Aerospace, Beltsville, Maryland.

^{††}The Aerospace Corporation, El Segundo, California.

Like a spacecraft's temperature, Earth's temperature is the result of a balance between absorbed and emitted energy. If one considers Earth and its atmosphere as a whole and computes averages of absorbed and outgoing energy over long time periods, one finds that the absorbed solar energy and the IR radiant energy emitted by Earth are essentially in balance; Earth is therefore very nearly in radiative equilibrium with the sun and deep space. However, the forms of energy are not in balance everywhere on the globe at all times, and important variations are found with respect to local time, geography, and atmospheric conditions.

In low Earth orbit (LEO), a space vehicle's altitude is small compared to the diameter of Earth. This means that a satellite views only a small portion of the full globe at any given time. The satellite's motion as it orbits therefore exposes it to rapidly changing environmental conditions as it passes over regions having different combinations of land, ocean, snow, and cloud cover. These short-duration swings in environmental conditions are not of much concern to massive, well-insulated spacecraft components. Exposed lightweight components such as solar arrays and deployable radiators, however, will respond to the extreme environments that are encountered for short time periods, so one must consider those environments in the design process. As the following discussion shows, the shorter the thermal time constant a particular component has, the wider the range of environments that must be considered.

Direct Solar

Sunlight is the greatest source of environmental heating incident on most spacecraft in Earth orbit. Fortunately, the sun is a very stable energy source. Even the 11-year solar cycle has very little effect on the radiation emitted from the sun, which remains constant within a fraction of 1% at all times. However, because Earth's orbit is elliptical, the intensity of sunlight reaching Earth varies approximately $\pm 3.5\%$, depending on Earth's distance from the sun. At summer solstice, Earth is farthest from the sun, and the intensity is at its minimum value of 1322 W/m^2 ; at winter solstice, the intensity is at its maximum of 1414 W/m^2 . The intensity of sunlight at Earth's mean distance from the sun (1 AU) is known as the solar constant and is equal to 1367 W/m^2 . The above values are recommended by the World Radiation Center in Davos, Switzerland,^{2,1,2,2} and are believed accurate to within 0.4%.

Solar intensity also varies as a function of wavelength, as shown in Fig. 2.2. The energy distribution is approximately 7% ultraviolet, 46% visible, and 47% near (short-wavelength) IR, with the total integrated energy equal to the 1322 to 1414 W/m^2 values mentioned above. An important point, however, is that the IR energy emitted by the sun is of a much shorter wavelength than that emitted by a body near room temperature. This distinction allows for the selection of thermal-control finishes that are very reflective in the solar spectrum but whose emissivity is high in the room-temperature (long-wavelength) IR portion of the spectrum, as shown in Fig. 2.3. These finishes minimize solar loads while maximizing a spacecraft's ability to reject waste heat. They are discussed in more detail in Chapter 4.

Albedo

Sunlight reflected off a planet or moon is known as albedo. A planet's albedo is usually expressed as the fraction of incident sunlight that is reflected back to space,

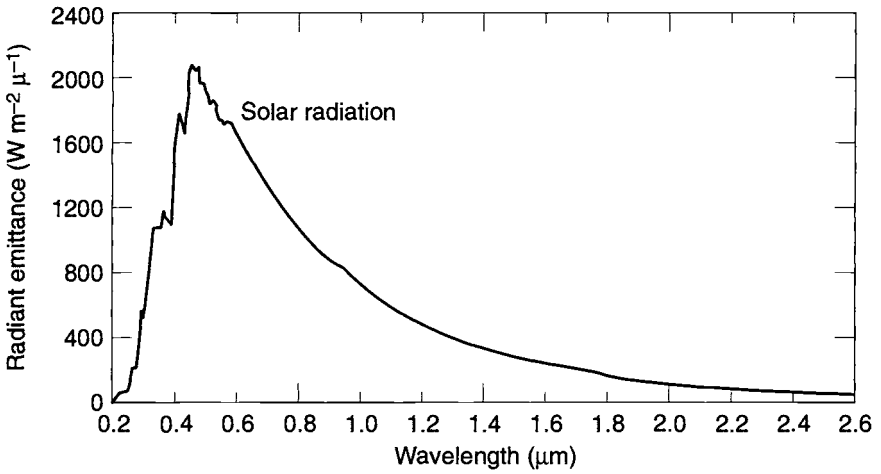


Fig. 2.2. Solar spectral distribution.

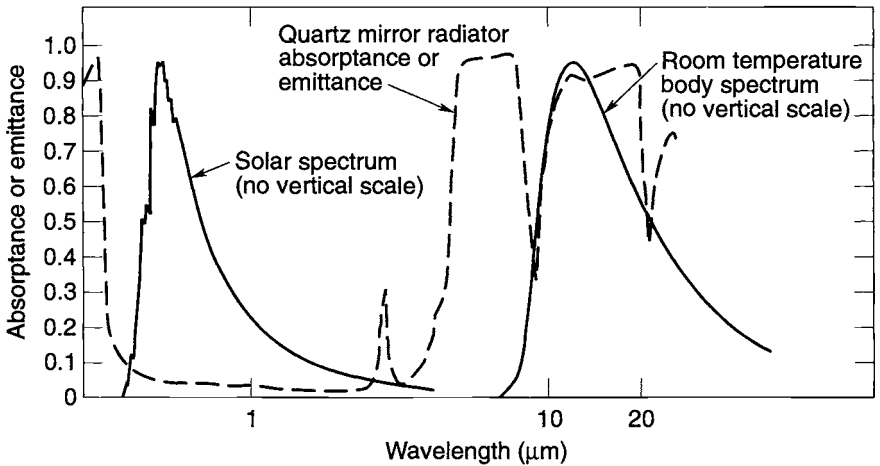


Fig. 2.3. Solar and room-temperature-body spectral distributions.

and it is highly variable. Usually, reflectivity is greater over continental regions than oceanic regions and generally increases with decreasing local solar-elevation angles and increasing cloud coverage. Because of greater snow and ice coverage, decreasing solar-elevation angle, and increasing cloud coverage, albedo also tends to increase with latitude. These variations make selection of the best albedo value for a particular thermal analysis rather uncertain, and variations throughout the industry are not unusual.

Another important point is that the albedo heat flux reaching a spacecraft will decrease as the spacecraft moves along its orbit and away from the subsolar point (the point on Earth or another planet where the sun is at the zenith, i.e., directly overhead), even if the albedo constant remains the same. This happens because the albedo factor is a reflectivity, not a flux. As the spacecraft moves away from the subsolar point it is over regions of Earth's surface where the local incident solar energy per square meter is decreasing with the cosine of the angle from the subsolar point. The albedo heat load on the spacecraft will therefore approach 0 near the terminator (the dividing line between the sunlit and dark sides of a planet), even if the albedo value (reflectivity) is 1.0. This geometric effect is accounted for by the analysis codes used to perform spacecraft thermal analysis. The analyst is just responsible for selecting the albedo (reflectivity) value itself.

Earth IR

All incident sunlight not reflected as albedo is absorbed by Earth and eventually reemitted as IR energy. While this balance is maintained fairly well on a global annual average basis, the intensity of IR energy emitted at any given time from a particular point on Earth can vary considerably depending on factors such as the local temperature of Earth's surface and the amount of cloud cover. A warmer surface region will emit more radiation than a colder area. Generally, highest values of Earth-emitted IR will occur in tropical and desert regions (as these are the regions of the globe receiving the maximum solar heating) and will decrease with latitude. Increasing cloud cover tends to lower Earth-emitted IR, because cloud tops are cold and clouds effectively block upwelling radiation from Earth's warmer surface below. These localized variations in Earth-emitted IR, while significant, are much less severe than the variations in albedo.

The IR energy emitted by Earth, which has an effective average temperature around -18°C , is of approximately the same wavelength as that emitted by spacecraft; that is, it is of much longer wavelength than the energy emitted by the sun at 5500°C . Unlike short-wavelength solar energy, Earth IR loads incident on a spacecraft cannot be reflected away from radiator surfaces with special thermal-control coatings, since the same coatings would prevent the radiation of waste heat away from the spacecraft. Because of this, Earth-emitted IR energy can present a particularly heavy backload on spacecraft radiators in low-altitude orbits.

The concept of Earth-emitted IR can be confusing, since the spacecraft is usually warmer than the effective Earth temperature, and the net heat transfer is from spacecraft to Earth. However, for analysis, a convenient practice is to ignore Earth when calculating view factors from the spacecraft to space and to assume that Earth does not block the view to space. Then the difference in IR energy is added back in as an "incoming" heat rate called Earth-emitted IR.

Recommended Values for Earth IR and Albedo

References 2.3 through 2.13 document early studies of albedo and Earth IR and contain detailed data pertaining to their variations, as measured by satellite-based sensors. Most of these early studies recommended design values for Earth IR and albedo based on monthly averages of the satellite data. These recommendations were made because of the unreasonableness of recommending that all spacecraft

hardware be designed to accommodate the short-term, extreme values of albedo and Earth IR resulting from local surface and atmospheric conditions.

Unfortunately, most spacecraft hardware has a thermal time constant on the order of minutes to a few days, not months. In the early 1990s, the International Space Station (ISS) program recognized that the monthly average thermal environments generally used by the satellite design community were not sufficient for designing safety-critical, short thermal-time-constant components such as the station's deployable radiators. NASA therefore funded studies at the Marshall Space Flight Center (MSFC) to improve the understanding of the LEO thermal environment for ISS and other spacecraft programs.^{2,14} This work was updated in 2001 by Anderson, Justus, and Batts.^{2,15}

The albedo and Earth IR values recommended here are based on the NASA/MSFC study, which considered 28 data sets of 16-second-resolution satellite sensor data collected monthly from the Earth Radiation Budget Experiment (ERBE). ERBE is a multisatellite experiment that has as its primary objective the global data collection of such Earth radiation budget parameters as incident sunlight, albedo, and Earth-emitted IR. This experiment was selected as a data source because of its thorough coverage and high-quality data from active-cavity, flat-plate radiometers in a fixed (nonscanning) wide-field-of-view mode. This type of instrument directly measures the albedo and Earth IR as a spacecraft surface would receive them. The sensors flew on an ERBE satellite in a low-inclination, 610-km-altitude orbit and on the National Oceanic and Atmospheric Administration (NOAA) 9 and 10 satellites in high-inclination, 849- and 815-km-altitude orbits, respectively. The sensor measurements were adjusted for altitude to derive effective albedo and IR values at the top of the atmosphere, which was assumed to be 30 km above Earth's surface. Therefore, in conducting a thermal analysis, one would use the environmental constants reported here with the Earth radius modeled as 6408 km. (However, if the actual equatorial radius of 6378 km were used instead of the top-of-the-atmosphere radius, the error would be less than 1%, which is not very significant compared to other analysis uncertainties.)

The MSFC study performed a statistical analysis of the ERBE data to identify the maximum and minimum albedo and Earth IR heating rates a spacecraft might be exposed to on orbit over various time periods from 16 sec to 24 h. The time periods were selected to encompass the range of thermal time constants found in most spacecraft hardware. (The values do not change significantly for periods greater than 24 h.) Ideally, such a study would provide the analyst with both an environmental heating rate and the probability that the value would not be exceeded over the duration of the spacecraft's mission. Unfortunately, this would require a statistical data set covering a time period that is very long compared to a spacecraft's design life. Because of the limited data set available, results are reported here according to the percentage of the time that one can expect the value will be exceeded on orbit. That is, the values shown will probably be exceeded during the mission, but not very often. Tables 2.1 and 2.2 summarize a conservative (3.3- σ) set of recommended albedo and Earth IR values that will be exceeded only 0.04% of the time, while Tables 2.3 and 2.4 give less severe (2- σ) values that will be exceeded 5% of the time.

**Table 2.1. Earth IR and Albedo^a, 3.3- σ Values^b
Cold Case**

Surface Sensitivity	Time Period	Inclination (deg)					
		0-30		30-60		60-90	
		Albedo	IR (W/m ²)	Albedo	IR (W/m ²)	Albedo	IR (W/m ²)
Albedo	16 sec	0.06	273	0.06	273	0.06	273
	128 sec	0.06	273	0.06	273	0.06	273
	896 sec	0.07	265	0.08	262	0.09	264
	30 min	0.08	261	0.12	246	0.13	246
	90 min	0.11	258	0.16	239	0.16	231
	6 h	0.14	245	0.18	238	0.18	231
	24 h	0.16	240	0.19	233	0.18	231
	IR	16 sec	0.40	150	0.40	151	0.40
128 sec		0.38	154	0.38	155	0.38	111
896 sec		0.33	173	0.34	163	0.33	148
30 min		0.30	188	0.27	176	0.31	175
90 min		0.25	206	0.30	200	0.26	193
6 h		0.19	224	0.31	207	0.27	202
24 h		0.18	230	0.25	210	0.24	205
Both albedo and IR		16 sec	0.13	225	0.15	213	0.16
	128 sec	0.13	226	0.15	213	0.16	212
	896 sec	0.14	227	0.17	217	0.17	218
	30 min	0.14	228	0.18	217	0.18	218
	90 min	0.14	228	0.19	218	0.19	218
	6 h	0.16	232	0.19	221	0.20	224
	24 h	0.16	235	0.20	223	0.20	224

^aAlbedo values shown on the table must be corrected to account for non-Lambertian reflection near the terminator. If orbit-average albedo is used in the analysis, the above values must be corrected according to orbit β angle (use table below). If the analysis changes the albedo value as the spacecraft moves about its orbit, the correction must be applied according to angle from subsolar point. (Use one correction or the other, not both.) No correction is needed for Earth IR.

^bValues exceeded 0.04% of the time.

Short-Term Albedo Correction		Orbit-Average Albedo Correction	
Position from Subsolar Point (deg)	Add Correction	Orbit β angle (deg)	Add Correction
0	none	0	0.04
20	0.02	20	0.05
40	0.04	40	0.07
50	0.05	50	0.09
60	0.08	60	0.12
70	0.13	70	0.16
80	0.20	80	0.22
90	0.31	90	0.31

**Table 2.2. Earth IR and Albedo^a, 3.3- σ Values^b
Hot Case**

Surface Sensitivity	Time Period	Inclination (deg)					
		0-30		30-60		60-90	
		Albedo	IR (W/m ²)	Albedo	IR (W/m ²)	Albedo	IR (W/m ²)
Albedo	16 sec	0.43	182	0.48	180	0.50	180
	128 sec	0.42	181	0.47	180	0.49	184
	896 sec	0.37	219	0.36	192	0.35	202
	30 min	0.33	219	0.34	205	0.33	204
	90 min	0.28	237	0.31	204	0.28	214
	6 h	0.23	248	0.31	212	0.27	218
	24 h	0.22	251	0.28	224	0.24	224
	IR	16 sec	0.22	331	0.21	332	0.22
128 sec		0.22	326	0.22	331	0.22	331
896 sec		0.22	318	0.22	297	0.20	294
30 min		0.17	297	0.21	282	0.20	284
90 min		0.20	285	0.22	274	0.22	250
6 h		0.19	269	0.21	249	0.22	221 ^c
24 h		0.19	262	0.21	245	0.20	217 ^c
Both albedo and IR		16 sec	0.30	298	0.31	267	0.32
	128 sec	0.29	295	0.30	265	0.31	262
	896 sec	0.28	291	0.28	258	0.28	259
	30 min	0.26	284	0.28	261	0.27	260
	90 min	0.24	275	0.26	257	0.26	244
	6 h	0.21	264	0.24	248	0.24	233
	24 h	0.20	260	0.24	247	0.23	232

^aAlbedo values shown on the table must be corrected to account for non-Lambertian reflection near the terminator. If orbit-average albedo is used in the analysis, the above values must be corrected according to orbit β angle (use table below). If the analysis changes the albedo value as the spacecraft moves about its orbit, the correction must be applied according to angle from subsolar point. (Use one correction or the other, not both.) No correction is needed for Earth IR.

^bValues exceeded 0.04% of the time.

^cFor orbits with β angles greater than 80 deg, increase this value by approximately 15 W/m².

Short-Term Albedo Correction		Orbit-Average Albedo Correction	
Position from Subsolar Point (deg)	Add Correction	Orbit β angle (deg)	Add Correction
0	none	0	0.04
20	0.02	20	0.05
40	0.04	40	0.07
50	0.05	50	0.09
60	0.08	60	0.12
70	0.13	70	0.16
80	0.20	80	0.22
90	0.31	90	0.31

**Table 2.3. Earth IR and Albedo^a, 2- σ Values^b
Cold Case**

Surface Sensitivity	Time Period	Inclination (deg)					
		30		60		90	
		Albedo	IR (W/m ²)	Albedo	IR (W/m ²)	Albedo	IR (W/m ²)
Albedo	16 sec	0.09	270	0.10	267	0.10	267
	128 sec	0.09	267	0.10	265	0.10	265
	896 sec	0.10	261	0.13	252	0.14	252
	30 min	0.12	257	0.16	242	0.17	244
	90 min	0.13	249	0.18	238	0.18	230
	6 h	0.15	241	0.19	233	0.19	230
	24 h	0.16	240	0.19	235	0.19	230
	IR	16 sec	0.30	195	0.33	183	0.35
128 sec		0.29	198	0.33	184	0.34	164
896 sec		0.26	209	0.28	189	0.27	172
30 min		0.23	216	0.25	200	0.25	190
90 min		0.20	225	0.23	209	0.24	202
6 h		0.18	231	0.23	212	0.23	205
24 h		0.17	233	0.23	212	0.23	207
Both albedo and IR		16 sec	0.15	236	0.19	227	0.20
	128 sec	0.16	237	0.19	227	0.20	225
	896 sec	0.16	237	0.20	226	0.20	227
	30 min	0.16	237	0.20	225	0.20	226
	90 min	0.16	237	0.20	225	0.21	224
	6 h	0.17	237	0.20	226	0.21	226
	24 h	0.17	236	0.20	226	0.20	225

^aAlbedo values shown on the table must be corrected to account for non-Lambertian reflection near the terminator. If orbit-average albedo is used in the analysis, the above values must be corrected according to orbit β angle (use table below). If the analysis changes the albedo value as the spacecraft moves about its orbit, the correction must be applied according to angle from subsolar point. (Use one correction or the other, not both.) No correction is needed for Earth IR.

^bValues exceeded 5% of the time.

Short-Term Albedo Correction		Orbit-Average Albedo Correction	
Position from Subsolar Point (deg)	Add Correction	Orbit β angle (deg)	Add Correction
0	none	0	0.04
20	0.02	20	0.05
40	0.04	40	0.07
50	0.05	50	0.09
60	0.08	60	0.12
70	0.13	70	0.16
80	0.20	80	0.22
90	0.31	90	0.31

**Table 2.4. Earth IR and Albedo^a, 2- σ Values^b
Hot Case**

Surface Sensitivity	Time Period	Inclination (deg)					
		30		60		90	
		Albedo	IR (W/m ²)	Albedo	IR (W/m ²)	Albedo	IR (W/m ²)
Albedo	16 sec	0.29	205	0.36	201	0.38	197
	128 sec	0.29	211	0.35	202	0.37	199
	896 sec	0.26	225	0.29	213	0.28	213
	30 min	0.24	234	0.27	223	0.26	223
	90 min	0.22	246	0.26	229	0.24	219
	6 h	0.20	252	0.25	231	0.23	224
	24 h	0.20	252	0.25	232	0.23	224
	IR	16 sec	0.17	285	0.17	280	0.17
128 sec		0.17	284	0.17	279	0.17	279
896 sec		0.18	279	0.18	264	0.18	263
30 min		0.18	274	0.20	258	0.20	258
90 min		0.19	268	0.21	254	0.21	242
6 h		0.19	261	0.21	242	0.21	216 ^c
24 h		0.18	258	0.21	241	0.21	215 ^c
Both albedo and IR		16 sec	0.21	260	0.23	240	0.24
	128 sec	0.21	260	0.23	240	0.24	238
	896 sec	0.21	261	0.23	241	0.23	240
	30 min	0.21	258	0.23	240	0.23	242
	90 min	0.20	258	0.23	241	0.23	232
	6 h	0.19	255	0.23	242	0.22	230
	24 h	0.19	257	0.23	241	0.23	230

^aAlbedo values shown on the table must be corrected to account for non-Lambertian reflection near the terminator. If orbit-average albedo is used in the analysis, the above values must be corrected according to orbit β angle (use table below). If the analysis changes the albedo value as the spacecraft moves about its orbit, the correction must be applied according to angle from subsolar point. (Use one correction or the other, not both.) No correction is needed for Earth IR.

^bValues exceeded 5% of the time.

^cFor orbits with β angles greater than 80 deg, increase this value by approximately 15 W/m².

Short-Term Albedo Correction		Orbit-Average Albedo Correction	
Position from Subsolar Point (deg)	Add Correction	Orbit β angle (deg)	Add Correction
0	none	0	0.04
20	0.02	20	0.05
40	0.04	40	0.07
50	0.05	50	0.09
60	0.08	60	0.12
70	0.13	70	0.16
80	0.20	80	0.22
90	0.31	90	0.31

The decision whether to use the 2- σ or 3.3- σ values for a given thermal design analysis should be based on the program's tolerance for risk, the consequences of a predicted temperature being occasionally exceeded, and the impact of conservatism on program cost and design complexity. Comparing the tables, however, reveals a difference that is not very large between the 2- and 3.3- σ values for components with time constants on the order of 90 min or more. As a further point of reference, a commonly used analysis-uncertainty margin of 10°C (see Chapter 15) corresponds to roughly a 2- σ protection against a predicted temperature being exceeded. For the rare instances in which a critical lightweight component (such as a tether) would break if exposed to an extreme environment even once, note that the worst measurements in the database exceeded the 3.3- σ values of Tables 2.1 and 2.2 by 17 W/m² for Earth IR and 0.06 for albedo for the 16-sec and 128-sec measurement periods.

During the study, it became apparent that the albedo and Earth IR values were dependent not only on the time period considered, but on the orbit inclination, orbit beta angle, and angle from the subsolar point as well (see pp. 36–43 for definition and discussion of these orbital parameters). Orbit-average Earth IR, for instance, is lower for high-inclination orbits because the satellite spends a significant amount of time over the cooler polar regions. Albedo, on the other hand, tends to increase at large angles from the subsolar point because sunlight is reflected off Earth with more forward scatter at the low angles of incidence that occur closer to the terminator. (The albedo is more Lambertian, or equal in all directions, closer to the subsolar point.) This latter effect causes the orbit-average albedo factor to increase for higher beta-angle orbits that keep the spacecraft closer to the terminator than the subsolar point during the sunlit portion of the orbit. An important point to note is that the correction factor shown in Tables 2.1 through 2.4 must be added to the tabulated albedo values to account for this effect.

Over the years some have questioned the appropriateness of using both the highest albedo and highest IR when performing a hot-case spacecraft thermal analysis, or both the lowest albedo and lowest IR when performing a cold-case analysis. The rationale is that if albedo is high, then the local Earth temperature, and therefore emitted planetary IR, must be low because so much sunlight is being reflected. The MSFC study shows that this reasoning is valid to some extent. As illustrated by the contour plots of 128-second data shown in Fig. 2.4, albedo and Earth IR are partially correlated. Low Earth IR values tend to be associated with high albedo while high Earth IR tends to be associated with low-to-moderate albedo. To address this issue, the MSFC study sorted the data in such a way that unrealistically severe combinations of the two parameters were avoided. To do this, the study used pairs of albedo and IR measurements taken at the same time on the same spacecraft. To select an appropriate albedo to use with a 3.3- σ hot Earth IR value, for example, analysts considered only those albedo measurements taken at the same time as the IR measurements that were at the 99.96 percentile (3.3- σ) level and above. Just the albedos associated with those hottest IR measurements were then averaged to come up with a reasonable combination of the two environmental parameters. This process was used to select the Earth IR-albedo pairs shown in Tables 2.1 through 2.4.

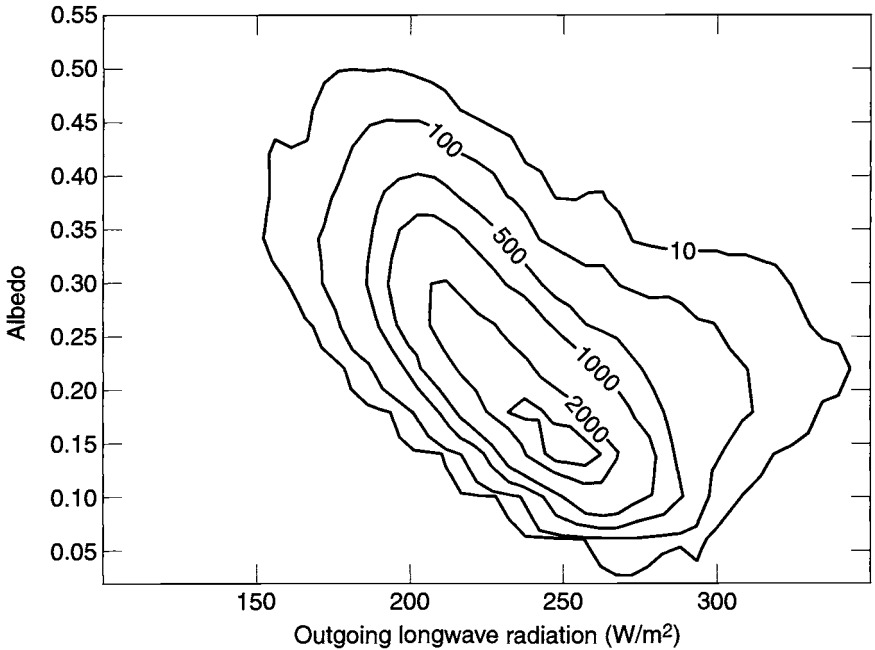


Fig. 2.4. Albedo-Earth IR pairs for medium-inclination orbits, 128-second data. (Contour intervals indicate relative frequency of occurrence.)

In selecting the appropriate hot- and cold-case albedo and Earth IR values for a particular thermal analysis, the analyst should also consider how sensitive the principal exposed surfaces are to IR versus solar energy. Most spacecraft radiator finishes, for example, have a low absorptance (say 0.2) and high emittance (around 0.8) and will therefore be much less sensitive to solar-wavelength albedo than to Earth-emitted IR. To enable better definition of the appropriate environmental constants for a particular analysis, Tables 2.1 through 2.4 contain recommended values for designs that are predominantly sensitive to either IR or albedo, or equally sensitive to both. In Tables 2.3 and 2.4, for instance, the values listed for IR-sensitive surfaces represent the 2- σ high and low Earth IR values along with the *average* albedos that occur during these extreme IR conditions.

Occasionally, one will come across a sensor or other component that requires extreme temperature stability over some period of time. In such situations, one must consider the rapid fluctuations in environmental heating that the device may see as it moves along its orbit. Figure 2.5 shows how Earth IR varied over one particular three-hour period. A low-mass device with a good radiative coupling to these environmental fluctuations might exceed a temperature-stability limit that is particularly tight. Such cases need to be evaluated on an individual basis considering the range of environments for various time periods shown in Tables 2.1 through 2.4.

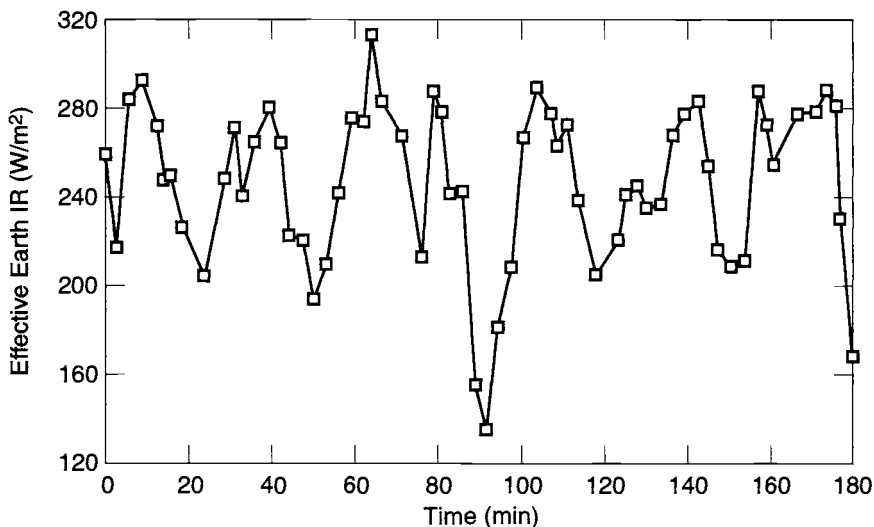


Fig. 2.5. Earth IR seen over a three-hour period by a spacecraft in LEO.

Free Molecular Heating

Another significant form of environmental heating is free molecular heating (FMH). This kind of heating is a result of bombardment of the vehicle by individual molecules in the outer reaches of the atmosphere. For most spacecraft, FMH is only encountered during launch ascent just after the booster's payload fairing is ejected. A desirable practice is to drop the fairing as soon as possible after launch to minimize the amount of dead weight the booster must deliver to orbit. The point at which the fairing is separated is often determined by a trade-off between the desire to save weight and the need to protect the payload spacecraft from excessive atmospheric heating.

Fairing separation always occurs at altitudes high enough for the resultant heating to be in the free or near-free molecular regime; that is, the heating is modeled as collisions of the body with individual molecules rather than as a gas-flow heating problem. The heating rate is given by:

$$Q_{\text{FMH}} = \alpha \left(\frac{1}{2} \right) \rho V^3 \quad (2.1)$$

where ρ is atmospheric density, V is vehicle velocity, and α is the accommodation coefficient (approximately 0.6 to 0.8, but a value of 1.0 is recommended for conservatism).

Atmospheric density is a highly variable parameter governed by a number of factors that cause the upper atmosphere to expand or contract. These factors include the level of solar electromagnetic activity ("F10.7," measured at a wavelength of 10.7 cm); the geomagnetic index (A_p); the longitude, latitude, and local

hour of the point in question; altitude; and day of the year. Atmospheric densities are calculated today using sophisticated atmospheric models with a dozen or more input parameters. The outputs of these models are atmospheric densities that will not be exceeded with a particular level of confidence (usually 97%). The output is expressed probabilistically because the level of solar activity, which is a major factor, is not predictable precisely.

The velocity of the vehicle relative to the atmosphere can be calculated in a rather straightforward manner for a satellite in orbit. The velocity during launch ascent, however, must be calculated using sophisticated booster-trajectory simulation programs that model and optimize the performance of the booster. Like atmospheric density, the trajectory and velocity of the booster are probabilistic, but to a lesser extent. The uncertainties are the result of variations in rocket-motor performance, guidance-system accuracies, high-altitude wind effects, and so on, and can result in the vehicle traveling at a different altitude or velocity than expected at any given time.

The atmospheric modeling and trajectory simulations are generally conducted by specialists in those areas, who then supply the thermal engineer with curves of worst-case heating versus time. With such a curve and a knowledge of the spacecraft attitude relative to the velocity vector, the thermal engineer may calculate the heat load on the spacecraft by simply multiplying the heating rate by the cross-sectional area of the surface in question and the cosine of the angle between the surface normal and velocity vector. A heating-rate curve for one particular mission during launch ascent is shown in Fig. 2.6.

As stated earlier, most spacecraft see FMH only during launch. Some spacecraft, however, have orbits with very low perigee altitudes and can therefore experience FMH in their operational orbits. In general, operational-orbit FMH rates should be assessed for any spacecraft with a perigee altitude below 180 km.

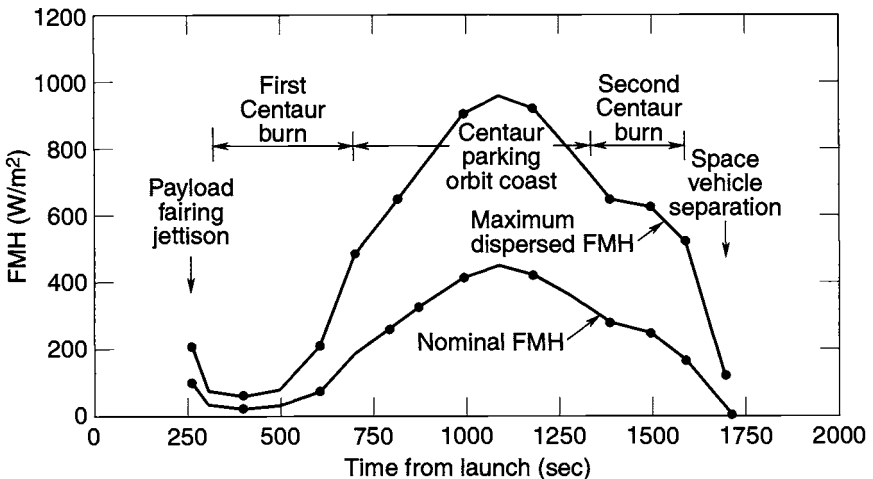


Fig. 2.6. Example of FMH profile.

Charged-Particle Heating

Charged particles constitute an additional heating source, although weak compared to the four principal environmental heating sources discussed above and generally not significant in the thermal design of room-temperature systems. At cryogenic temperatures, however, charged-particle heating can become a significant factor in thermal design because of the high sensitivity of such systems to environmental heat loads.

The near-Earth trapped charged particles, known as the Van Allen belts, lie about the plane of the geomagnetic equator and feature relativistic electrons and protons. The spatial characteristics of the Van Allen belts and the spectral properties of the trapped particles within them undergo both regular and irregular variations with time, accounted for by the solar-activity level. The bulk of the Van Allen belts is approximately bounded by altitudes of 6500 and 52,000 km. In 1958, Van Allen discovered the inner proton belt peaking in intensity at an approximate altitude of 9400 km, while Fan *et al.*,^{2.16} O'Brien *et al.*,^{2.17} and Dessier and Karplus^{2.18} helped to establish the existence of other electron peaks. Vette^{2.19} developed a complete mapping of the Van Allen belt radiations.

Standard trapped-particle environmental models include electron data for maximum and minimum solar-activity periods, an interim model for outer-zone electrons, and the maximum and minimum solar-activity model for energetic trapped protons. These data represent omnidirectional integral intensities averaged over periods in excess of 6 months in orbit. Over most regions of magnetospheric space, short-term excursions can vary from these values by factors of 100 to 1000, depending on particle energies and the type and intensity of the causative event.

Data on trapped proton and electron fluxes as functions of energy for circular, geomagnetic equatorial orbits ranging in altitude from 3200 to 35,800 km (synchronous) are presented in Fig. 2.7. As illustrated, the concentration of relativistic (> 5 MeV) protons is evident at lower altitudes (< 6400 km), while near synchronous altitude (35,800 km), proton energies are less than 2 MeV. Conversely, electrons feature high flux levels and energies less than approximately 5 MeV over a wide spectrum of altitudes.

The heating caused by these charged particles generally occurs in the first few hundredths of a centimeter of a material's thickness and is therefore essentially front-surface-absorbed, like solar, IR, or free molecular heating. Charged-particle heating rates, while not significant at room temperature, can significantly raise the equilibrium temperature of a cryogenic radiator, as shown in Fig. 2.8. A radiator designed for steady-state operation at 70 K in circular equatorial Earth orbit will warm to approximately 72.9 K for the charged-particle heating conditions at 3200 km altitude, while warming to 74.7 K and 70.4 K for the conditions at 6400 km and synchronous altitudes, respectively. In the theoretical limit where $T_{\text{equiv}} = 0$ K, the charged-particle heating effect will warm the radiator to approximately 27.3 K for the synchronous (35,800-km) circular equatorial Earth orbit condition. (The equilibrium temperature increase for the 19,100-km-altitude condition is nearly identical to the results for 3200 km, and therefore was not included in Fig. 2.8. For such systems, charged-particle heating must therefore be considered in the design and sizing of radiators. See Jimenez for a detailed discussion of this phenomenon.^{2.20})

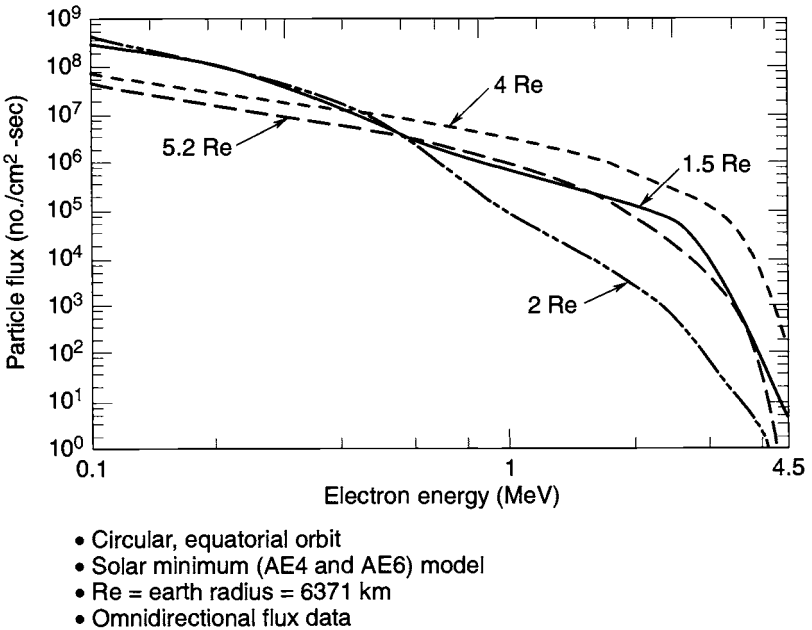
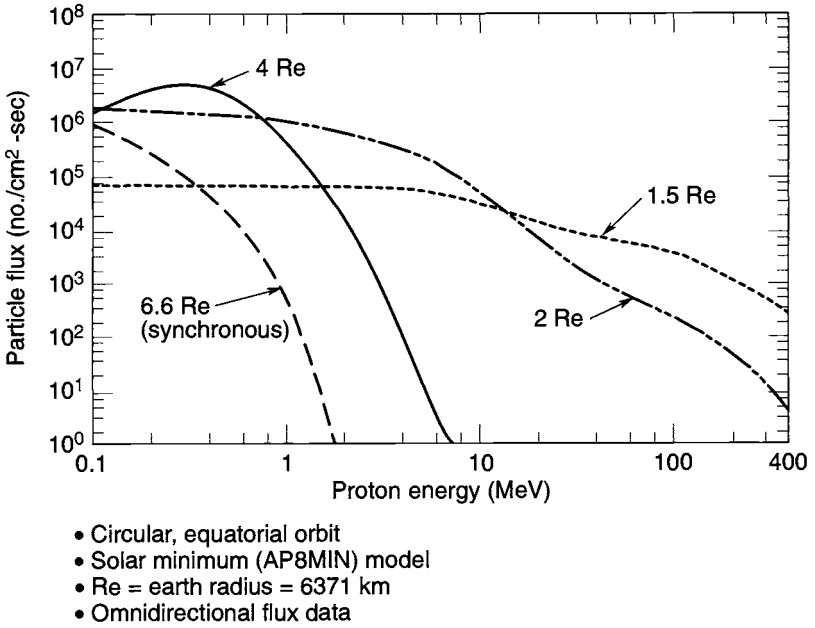


Fig. 2.7. Proton and electron flux for several Earth equatorial orbits.

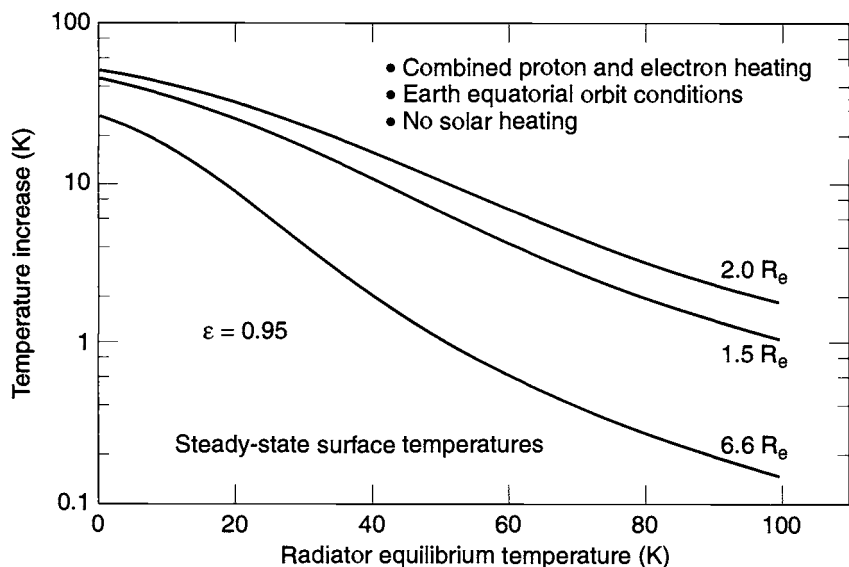


Fig. 2.8. Equilibrium temperature increase of an aluminum radiator as a result of natural environment charged-particle heating.

Standard Earth Orbits

In Chapter 1 the most common types of Earth orbits were described: LEO, geosynchronous (GEO), Molniya, and sun-synchronous. In this section, characteristics of the thermal environments encountered in each of these orbits will be discussed. Calculation of the actual heat loads that these environments impose on spacecraft surfaces will be addressed in Chapter 15.

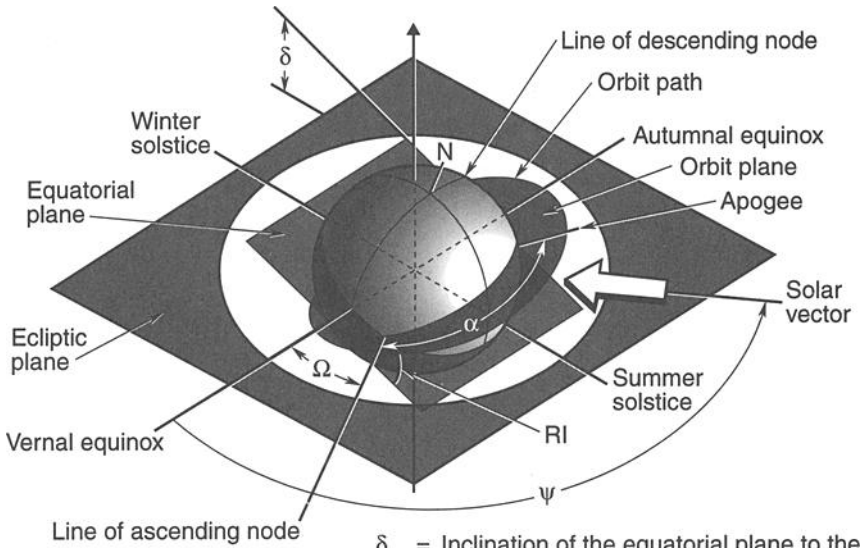
Terminology

To begin this discussion, some terminology definition is required. Several orbital parameters are commonly used in analyses of environmental heating. These are generally the same parameters used by orbit analysts to describe the spacecraft orbit, and their use simplifies the process of getting the inputs necessary to conduct the thermal analysis for any given program. The most important parameters are defined here and illustrated in Figs. 2.9 and 2.10.

Equatorial plane: the plane of Earth's equator, which is perpendicular to Earth's spin axis.

Ecliptic plane: The plane of Earth's orbit around the sun. From the point of view of Earth, the sun always lies in the ecliptic plane. Over the course of a year, the sun appears to move continuously around Earth in this plane. Because of the tilt of Earth's spin axis, the equatorial plane is inclined 23.4 deg from the ecliptic plane, shown in Fig. 2.9 as the angle δ .

Sun day angle: The position angle of the sun in the ecliptic plane measured from vernal equinox. At vernal equinox this angle is 0 deg, at summer solstice 90



- δ = Inclination of the equatorial plane to the ecliptic plane
- Ω = Right ascension of the ascending node
- α = Argument of apogee
- ψ = Sun day angle
- RI = Orbit inclination to the equatorial plane
- AA = $(R_a + R_p)/2$
- EE = $1 - R/AA$

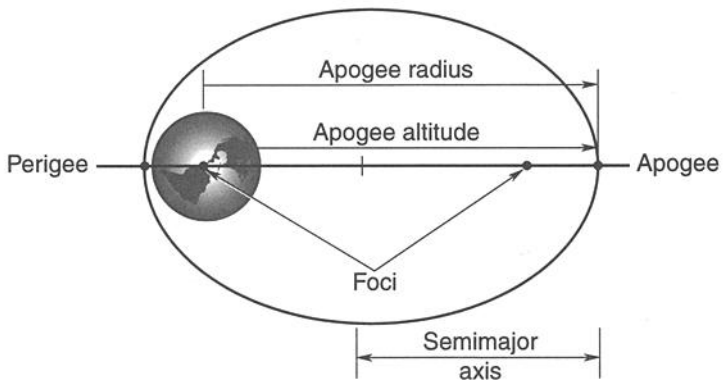


Fig. 2.9. Orbital parameters.

deg, at autumnal equinox 180 deg, and at winter solstice 270 deg. This angle is shown as ψ in Fig. 2.9 and should not be confused with the “right ascension” of the sun, which is measured in the equatorial plane and is slightly different on most days of the year.

Orbit inclination: The angle between the orbit plane and the equatorial plane, shown as RI in Fig. 2.9. Orbit inclinations typically vary from 0 to 98 deg, although inclinations greater than 98 deg are possible. For inclinations less than 90 deg, the satellite appears to be going around its orbit in the same direction as Earth’s rotation. For inclinations greater than 90 deg, it appears to be going opposite Earth’s rotation. In this case its orbit is known as a retrograde orbit.

Altitude: the distance of a satellite above Earth’s surface.

Apogee/perigee: Apogee is the point of highest altitude in an orbit; perigee, the lowest.

Ascending node/descending node: The ascending node is the point in the orbit at which the spacecraft crosses Earth’s equator while traveling from south to north (i.e., when it is “ascending”). The descending node is the point crossed during the southbound portion of the orbit.

Right ascension and declination: The position of an object in the celestial coordinate system (Fig. 2.10). Right ascension is the position angle in the equatorial plane measured from vernal equinox. Declination is the position angle above or below the equatorial plane.

Right ascension of the ascending node (RAAN): The position angle of the ascending node measured from vernal equinox in the equatorial plane (Ω in Fig. 2.9). Earth’s equatorial bulge causes the ascending and descending nodes to drift slightly on each revolution about Earth. (Earth is not a true sphere.) This drifting is known as “nodal regression.” For most orbits the RAAN drifts continuously with time and varies from 0 to 360 deg.

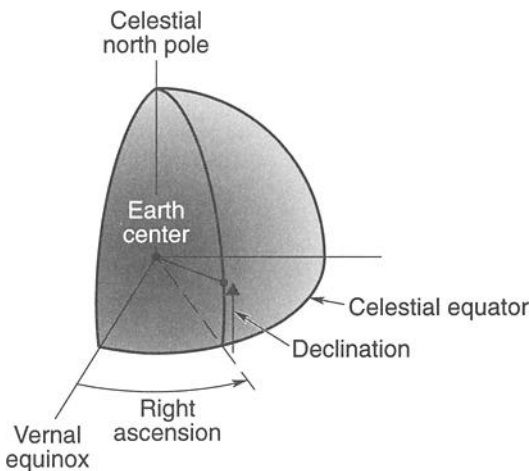


Fig. 2.10. Celestial coordinates.

Semimajor axis: the semimajor axis of the orbit ellipse.

$$a = \frac{r_a + r_p}{2}, \quad (2.2)$$

where a is the orbit semimajor axis, r_a is the orbit radius at apogee (Earth's radius + apogee altitude), and r_p is the orbit radius at perigee (Earth's radius + perigee altitude).

Period: The time required to make one revolution about the Earth. As orbit altitude increases, so does the period. The orbit period may be calculated using the relation

$$P = 2\pi \left(\frac{a^3}{\mu} \right)^{1/2}. \quad (2.3)$$

where P is the period, μ is the product of the universal gravitational constant and the mass of the planet (for Earth, $\mu = 3.98603 \times 10^{14} \text{ m}^3/\text{s}^2$), and a is the semimajor axis of the orbit (for a circular orbit, this is the orbit radius). The period of circular orbits versus orbit altitude is plotted in Fig. 2.11.

Eccentricity: The degree of oblateness of the orbit, defined as the ratio of one-half the interfocal distance to the semimajor axis. For a circular orbit, the eccentricity is 0. As the orbit becomes more elliptical, the eccentricity increases. Eccentricity is related to the apogee and perigee radii and the semimajor axis by the following relationships:

$$r_a = a(1 + e), \text{ and} \quad (2.4)$$

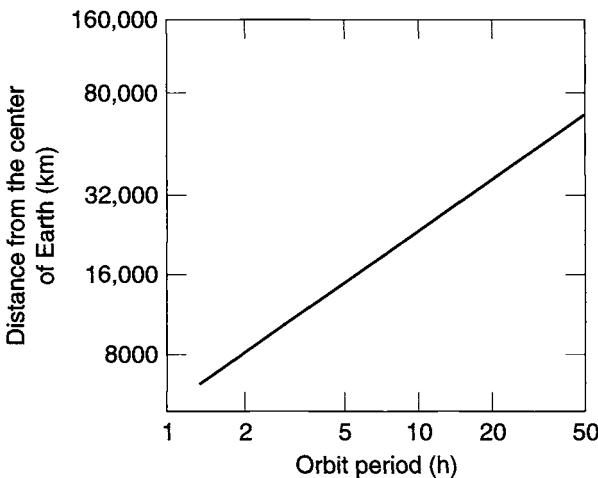


Fig. 2.11. Total amount of time per orbit.

$$r_p = a(1 - e), \quad (2.5)$$

where r_a is the orbit radius at apogee, r_p is the orbit radius at perigee, a is the orbit semimajor axis, and e is the eccentricity.

Argument of apogee: For an elliptical orbit, the angle between the ascending node and apogee measured in the direction of satellite motion. This angle, shown as α in Fig. 2.9, can vary from 0 to 360 deg.

Orbit Beta Angle

Although the above parameters are used by orbit and thermal analysts to describe particular orbits, another parameter, known as the orbit beta angle (β), is more useful in visualizing the orbital thermal environment, particularly for low Earth orbits. The orbit beta angle is the minimum angle between the orbit plane and the solar vector, and it can vary from -90 to $+90$ deg, as illustrated in Fig. 2.12(a). The beta angle is defined mathematically as

$$\beta = \sin^{-1}(\cos \delta_s \sin RI \sin(\Omega - \Omega_s) + \sin \delta_s \cos RI), \quad (2.6)$$

where δ_s is the declination of the sun, RI is the orbit inclination, Ω is the right ascension of the ascending node, and Ω_s is the right ascension of the sun.

As viewed from the sun, an orbit with β equal to 0 deg appears edgewise, as shown in Fig. 2.12(b). A satellite in such an orbit passes over the subsolar point on Earth where albedo loads (sunlight reflected from Earth) are the highest, but it also has the longest eclipse time because of shadowing by the full diameter of Earth. As β increases, the satellite passes over areas of Earth further from the subsolar point, thereby reducing albedo loads; however, the satellite is also in the sun for a larger percentage of each orbit as a result of decreasing eclipse times. At some point, which varies depending on the altitude of the orbit, eclipse time drops to 0. With β equal to 90 deg, a circular orbit appears as a circle as seen from the sun; no eclipses exist, no matter what the altitude; and albedo loads are near 0. Fig. 2.12(b) shows how orbits of various beta angles appear as seen from the sun. Note

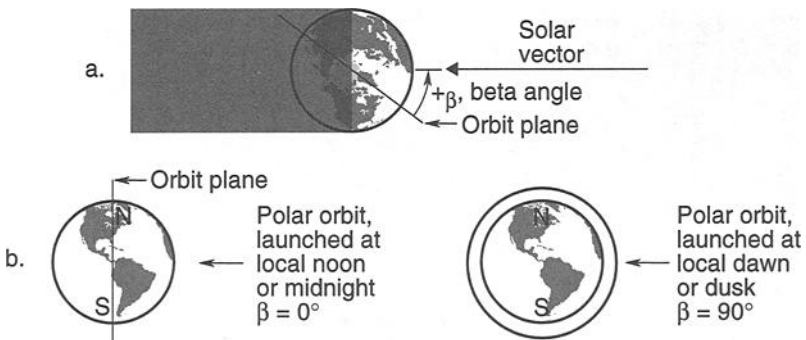


Fig. 2.12. Orbit beta angle.

that beta angles are often expressed as positive or negative; positive if the satellite appears to be going counterclockwise around the orbit as seen from the sun, negative if clockwise.

Figure 2.13 shows how eclipse times vary with β for circular orbits of different altitudes. The eclipse fraction of a circular orbit can be calculated from Eq. (2.7).

$$f_E = \frac{1}{180^\circ} \cos^{-1} \left[\frac{(h^2 + 2Rh)^{1/2}}{(R+h) \cos \beta} \right] \quad \text{if } |\beta| < \beta^* \quad (2.7)$$

$$= 0 \quad \text{if } |\beta| \geq \beta^*,$$

where R is Earth's radius (6378 km), h is orbit altitude, β is orbit beta angle, and β^* is the beta angle at which eclipses begin.

β^* may be calculated using Eq. (2.8), as follows:

$$\beta^* = \sin^{-1} \left[\frac{R}{(R+h)} \right] \quad 0^\circ \leq \beta^* \leq 90^\circ. \quad (2.8)$$

Both Eqs. (2.7) and (2.8) assume Earth's shadow is cylindrical, which is valid for low orbits where no appreciable difference exists between the umbral and penumbral regions of total and partial eclipsing, respectively. For 12-hour and geosynchronous orbits, these equations may be slightly in error.

For any given satellite, β will vary continuously with time because of the orbit nodal regression and the change in the sun's right ascension and declination over the year. The regression rates as a function of inclination for circular orbits of different altitudes are shown in Fig. 2.14. The sun's right ascension and declination throughout the year are shown in Fig. 2.15. The β history for a particular satellite

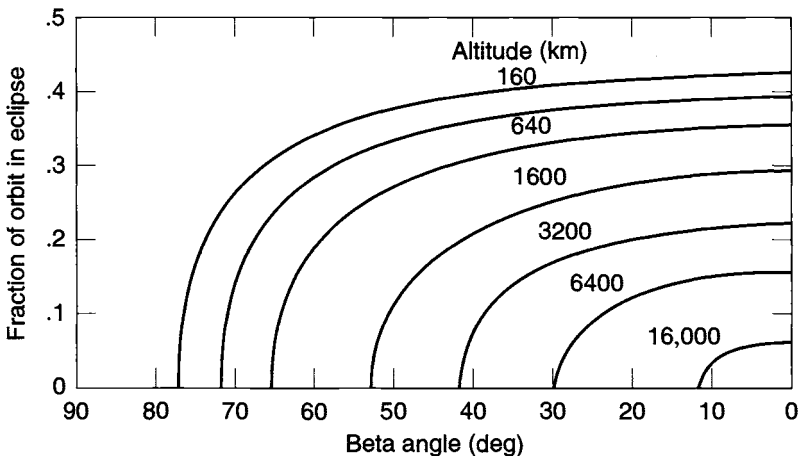


Fig. 2.13. Eclipse durations.

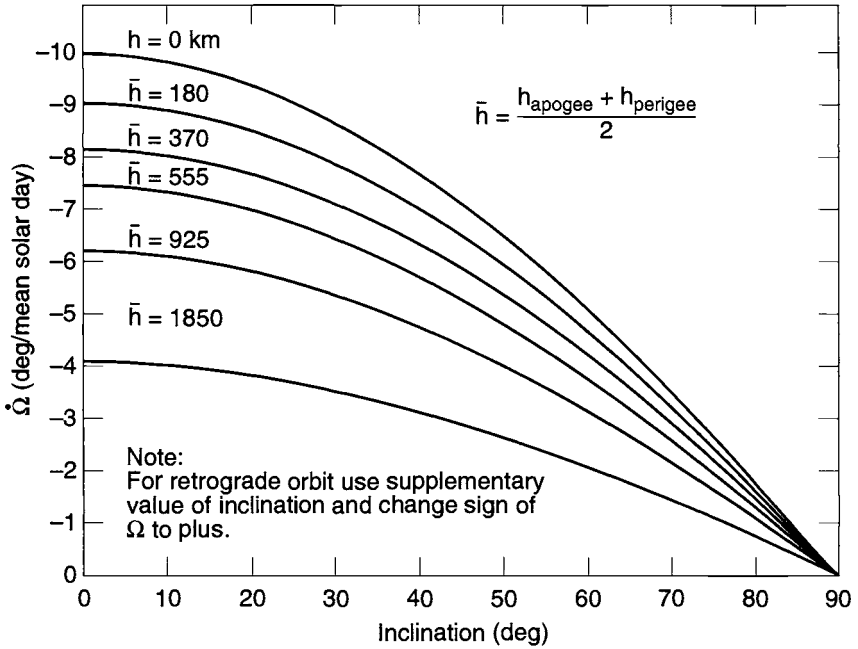


Fig. 2.14. Regression rate due to oblateness vs. inclination for various values of average altitude.

in a 500-km-altitude, circular orbit is shown in Fig. 2.16. The absolute value of β can vary from 0 to a maximum that equals the orbit inclination plus the maximum declination of the sun (i.e., inclination plus 23.4 deg).

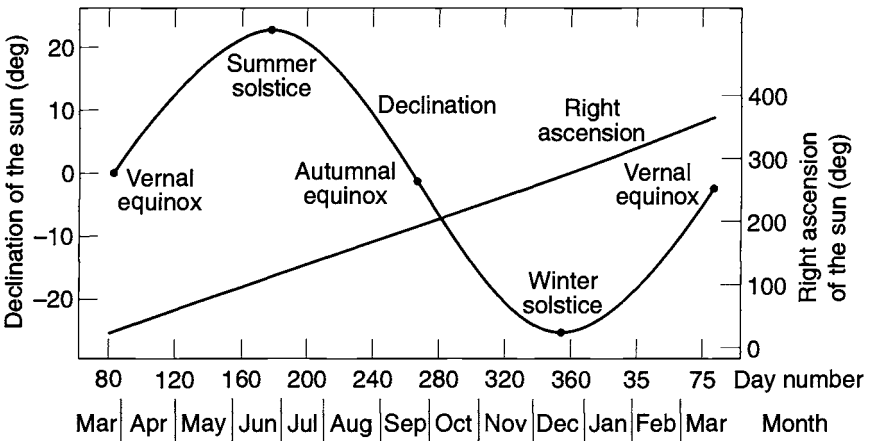


Fig. 2.15. Solar declination and right ascension vs. date.

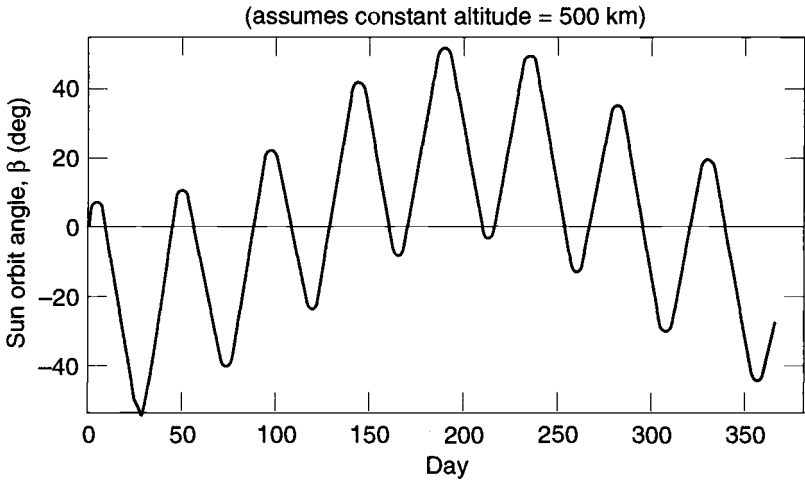


Fig. 2.16. Sample orbit-beta-angle drift (Lockheed Martin).

If the nodal regression of an orbit proceeds eastward at exactly the rate at which the sun's right ascension changes over the year, thereby "following" the sun, the orbit is called sun-synchronous. Because the sun moves uniformly eastward along the equator through 360 deg a year (about 365.242 mean solar days), the required rate of nodal regression is $360/365.242$, or 0.985647 deg/day. For circular orbits, sun-synchronism is possible for retrograde orbits (i.e., inclination > 90 deg) up to an altitude of about 5975 km.

The orbit inclination required to achieve sun-synchronism in circular orbits is shown as a function of orbit altitude in Fig. 2.17. Note that, because of the change in the sun's declination over the year, β is not constant but varies over a small range. The β histories for 833-km sun-synchronous orbits with different initial values for RAAN are shown in Fig. 2.18.

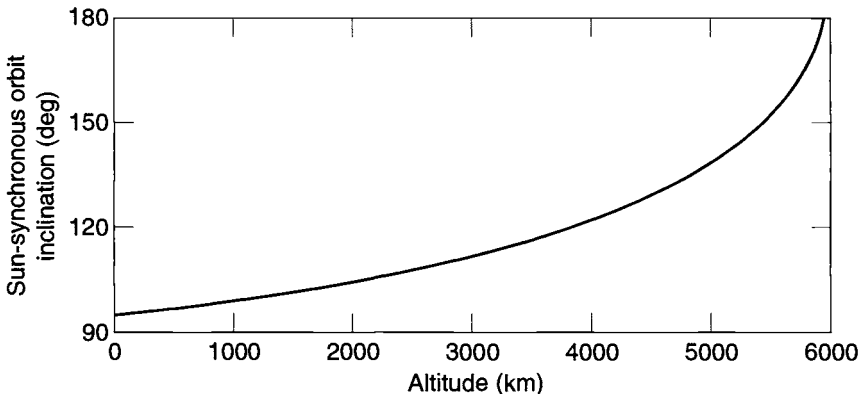


Fig. 2.17. Altitude vs. inclination for sun-synchronous orbits.

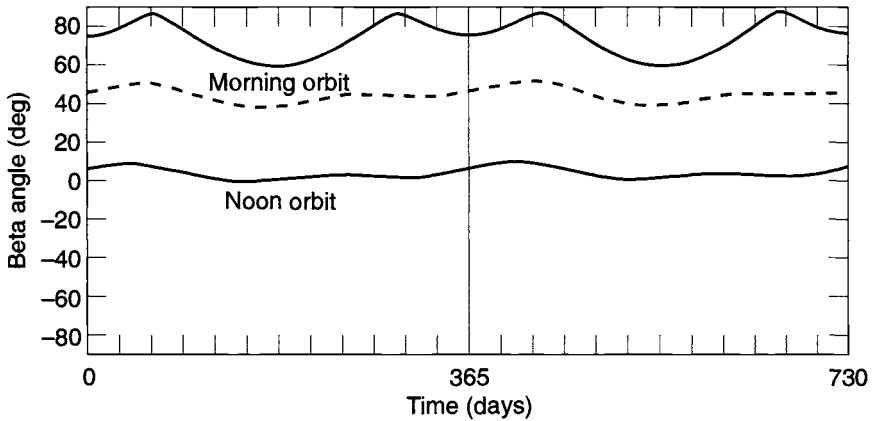


Fig. 2.18. Orbit-beta-angle histories for sun-synchronous, 833-km orbits.

Low Earth Orbits

The chief advantage in thinking in terms of β is that it simplifies the analysis of orbital thermal environments. By analyzing the environments at several discrete β values, one can be confident that all possible combinations of orbit RAAN and sun day angles have been covered. Figure 2.19 shows such an analysis for a spinning

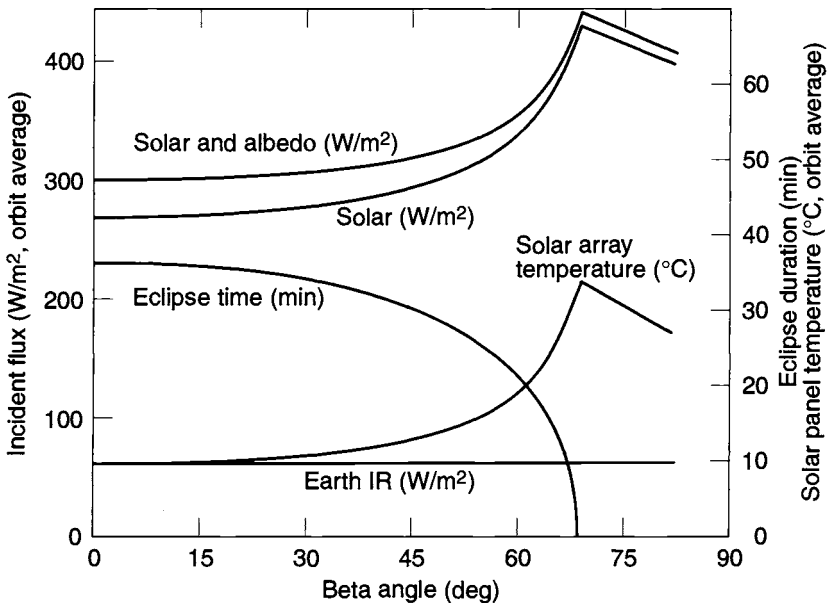


Fig. 2.19. Cylinder in low Earth orbit.

cylindrical satellite in a 555-km-altitude LEO. Earth-emitted IR was considered constant over Earth and therefore independent of orbit inclination, RAAN, or β . The IR load to the satellite therefore is constant with β . Since the eclipse time decreases with β , however, the satellite spends more time in the sun, thereby increasing the orbit-average solar load, as shown in Fig. 2.19. Also, as β increases, the albedo loads decrease, as can be seen by comparing the “solar” and “solar plus albedo” curves in Fig. 2.19. The net result for this particular satellite was that solar-panel orbit-average temperature (which provides a radiative heat sink for the internal components) was a minimum at $\beta = 0$ deg and a maximum at $\beta = 65$ deg.

Geosynchronous Orbits

As orbit altitude increases, environmental loads from Earth (IR and albedo) decrease rapidly. The graph in Fig. 2.20 shows these loads on a black plate over the subsolar point for various altitudes. By the time a spacecraft reaches GEO orbit, these loads are insignificant for most thermal-design analyses. The one exception to this rule is the case of cryogenic systems, which operate at such low temperatures that even small environmental heat loads from Earth are significant to the thermal design.

With such small Earth loads, the only significant environmental load for non-cryogenic systems in GEO orbit is solar. At this altitude the spacecraft is in the sun most of the time, and the maximum possible eclipse duration is only 72 minutes out of the 24-hour orbit. Since most GEO orbits have inclinations of less than 4 deg, eclipses occur only around vernal and autumnal equinox, in periods known as “eclipse seasons.” During summer and winter the sun’s declination causes Earth’s shadow to be cast above or below the satellite orbit, making eclipses impossible, as shown in Fig. 2.21. For circular, 24-hour orbits inclined by more than a few degrees, eclipses could occur during seasons other than equinox, but such orbits are rather rare and the maximum eclipse duration would be the same.

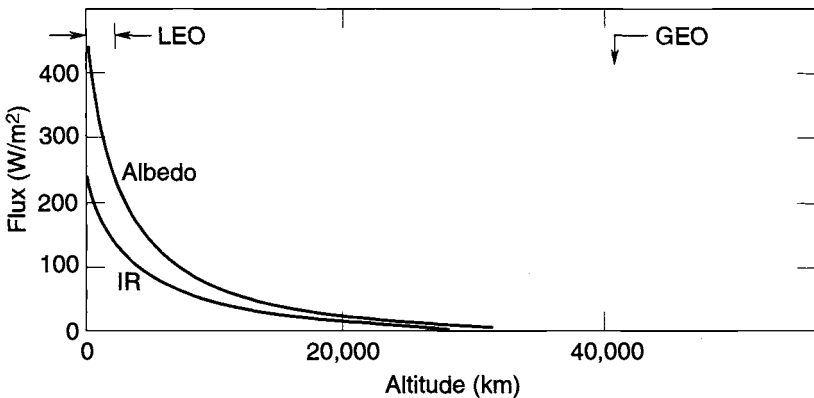


Fig. 2.20. Earth heat loads vs. altitude.

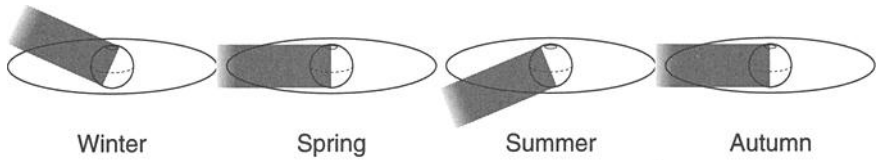


Fig. 2.21. GEO orbit eclipse, once per orbit, spring and autumn only (Northrop Grumman).

Many of the satellites in GEO orbit are the three-axis type, with one side of the vehicle constantly facing Earth, as shown in Fig. 2.22. For satellites such as this, the north and south faces receive the lowest peak solar flux, since the sun can only rise to a 23.4-deg angle above the surface (or maybe a little higher if the orbit has a slight inclination). As the spacecraft travels the orbit, the sun maintains a fixed elevation angle from these surfaces as the spacecraft rotates to always face Earth, as shown in Fig. 2.22. This elevation angle changes from +23.4 deg in summer (sun on the north surface) to -23.4 deg in winter (sun on the south surface). The other four surfaces will see the sun circle around them during the orbit, with the result of a cosine variation in intensity from no sun to a full sun normal to the surface. Because the sun can only rise to an angle of 23.4 deg “above” the north/south faces, the maximum solar load on these surfaces is $(\sin 23.4 \text{ deg}) (1.0 \text{ normal sun}) = 0.4 \text{ suns}$, while the maximum load on all the other faces is 1.0 sun. Therefore a common practice is to mount the highest-power dissipation components on the north and south faces, where the reduced solar loads make it easier to reject heat from the spacecraft.

The moon can also cause eclipses. These are far less frequent than Earth eclipses and are of shorter duration, so they are not thermal design drivers for most spacecraft. Furthermore, while Earth and the moon can physically cause consecutive eclipses, the probability of this actually occurring is extremely remote and is usually not considered in spacecraft thermal design. Nonetheless, an assessment of the impact of consecutive eclipses on vehicle survival is a good idea if the

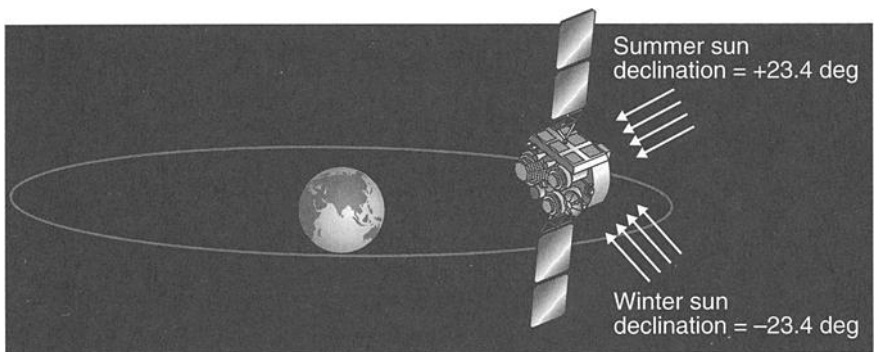


Fig. 2.22. Solar illumination of GEO satellite.

spacecraft orbit could result in such a condition. At least one spacecraft has unexpectedly encountered consecutive eclipses and, although the vehicle survived, its payload temperatures fell well below allowable limits.

Twelve-Hour Circular Orbits

The thermal environment in 12-hour circular orbits is much like that in GEO orbits. Earth loads (IR and albedo) are not significant unless cryogenic systems are involved, leaving solar loads as the only environmental loads. At this time, these orbits are being used primarily by the Global Positioning System (GPS) and its Russian counterpart, GLONASS (Global Navigation Satellite System). Both of these programs include a number of satellites in 12-hour circular orbits with many different inclinations.

The angles of solar illumination on spacecraft in 12-hour circular orbits, unlike the angles on GEO vehicles, can vary considerably with various orbit inclinations, but the maximum eclipse length is 56 minutes for all 12-hour circular orbits.

Molniya Orbits

Molniya orbits are unusual in that they have an extreme degree of eccentricity (i.e., they are very elliptical) and a high inclination (62 deg). With perigee altitudes in the LEO range of approximately 550 km and apogee altitudes of near GEO altitude (38,900 km), a spacecraft in such an orbit goes through a wide swing in thermal environments. Near perigee Earth loads are high, but at apogee only the solar loads are significant. Since its velocity is much higher near perigee, the spacecraft tends to spend most of the 12-hour orbit period at higher altitudes and relatively little time at low altitudes, where Earth loads are significant. Figure 2.23 shows the position of a spacecraft in a Molniya orbit at 1-hour intervals and a graph of Earth IR load versus time on a flat plate facing Earth to illustrate the environmental changes that occur around the orbit.

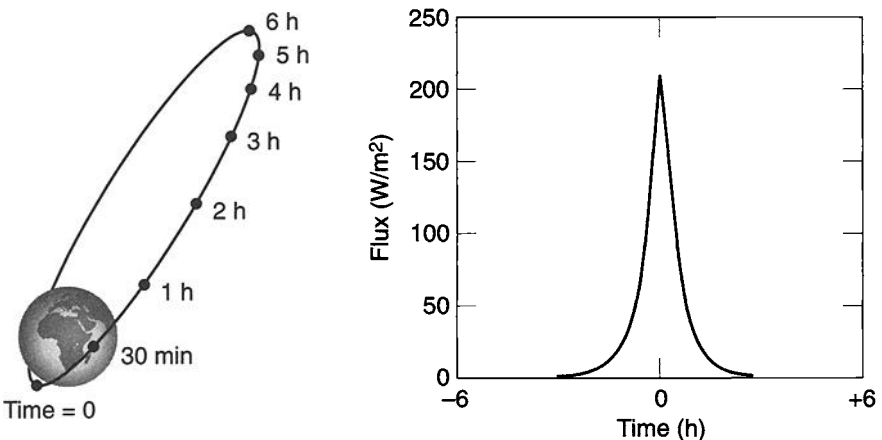


Fig. 2.23. Earth IR heating in Molniya orbit, flat black plate facing Earth.

Eclipse times for Molniya orbits vary considerably with season. During summer, spring, and fall, Earth's shadow is cast on the southern portion of the orbit, where the spacecraft is at low altitude and traveling very fast (see Fig. 2.24). This results in relatively short eclipse times. During the winter Earth's shadow is cast on more northerly portions of the orbit, where the spacecraft is at higher altitude and lower velocity; the result is longer eclipse times. The range of eclipse times for Molniya orbits is 0 (for high- β orbits) to 72 minutes for certain winter eclipses.

Environments of Interplanetary Missions

Environments of Interplanetary Cruises

Interplanetary cruise trajectories can expose spacecraft to a range of thermal environments much more severe than those encountered in Earth orbit. During most of an interplanetary cruise, the only environmental heating comes from direct sunlight. As noted in Chapter 1, some missions require close flybys past planets for a gravity-assisted change of velocity and direction. During a flyby, a spacecraft is exposed to IR and albedo loads from the planet. Table 2.5 provides the size and basic orbital characteristics of the planets and Earth's moon.

During an interplanetary cruise, a spacecraft's distance from the sun determines the thermal environment at all times except during planetary flybys. If the mean solar intensity near Earth is defined as 1 "sun," then a spacecraft would be exposed to 6.5 suns at the mean orbit of Mercury, but only 0.0006 suns at the mean orbit of Pluto/Charon. Equation 2.9 and Fig. 2.25 show solar flux as a function of distance from the sun in AU.

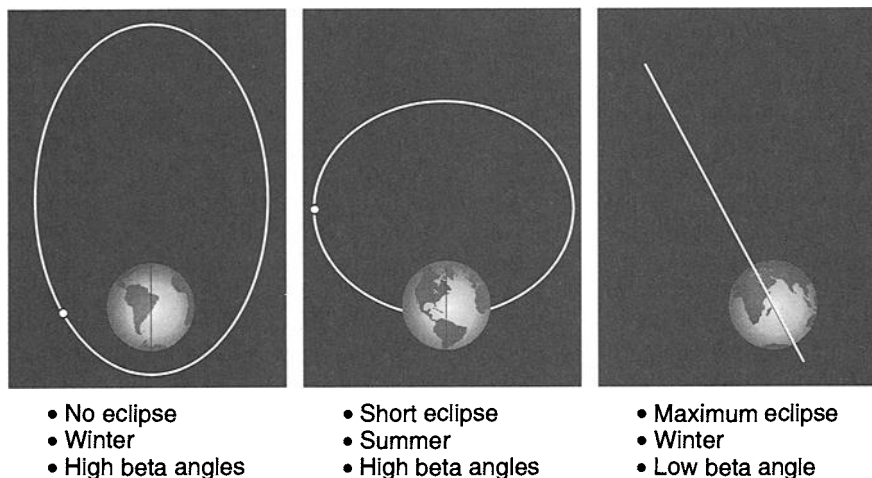


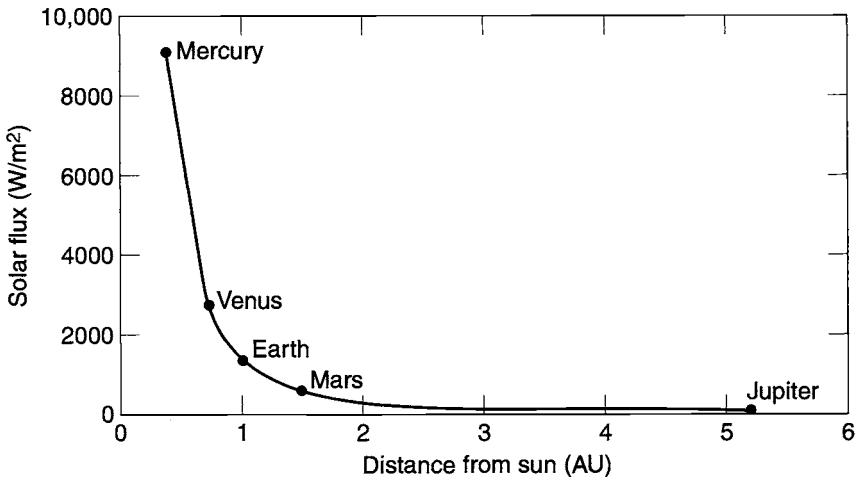
Fig. 2.24. Molniya eclipses.

Table 2.5. Planetary Size and Orbit Parameters

Planet	Orbit Semimajor Axis (AU)	Perihelion Distance (AU)	Aphelion Distance (AU)	Equatorial Radius (km)
Mercury	0.3871	0.3075	0.4667	2425
Venus	0.7233	0.7184	0.7282	6070
Earth	1.000	0.9833	1.0167	6378
Moon	1.000	0.9833	1.0167	1738
Mars	1.524	1.381	1.666	3397
Jupiter	5.20	4.95	5.45	71,300
Saturn	9.54	9.01	10.07	60,100
Uranus	19.18	18.28	20.09	24,500
Neptune	30.06	29.80	30.32	25,100
Pluto/Charon	39.44	29.58	49.30	3,200 (Pluto)

$$\text{Solar flux} = \frac{1367.5 \text{ W}}{\text{AU}^2 \text{ m}^2} \quad (2.9)$$

To give a feel for the thermal environments encountered during interplanetary missions, we will use the concept of a “reference sphere.” This reference will be an isothermal sphere with an absorptance and emittance of 1.0. The equilibrium temperature of the sphere will provide a rough indication of how “hot” or “cold” the local thermal environment is. Figure 2.26 shows the sphere’s equilibrium


Fig. 2.25. Solar flux as a function of distance from the sun.

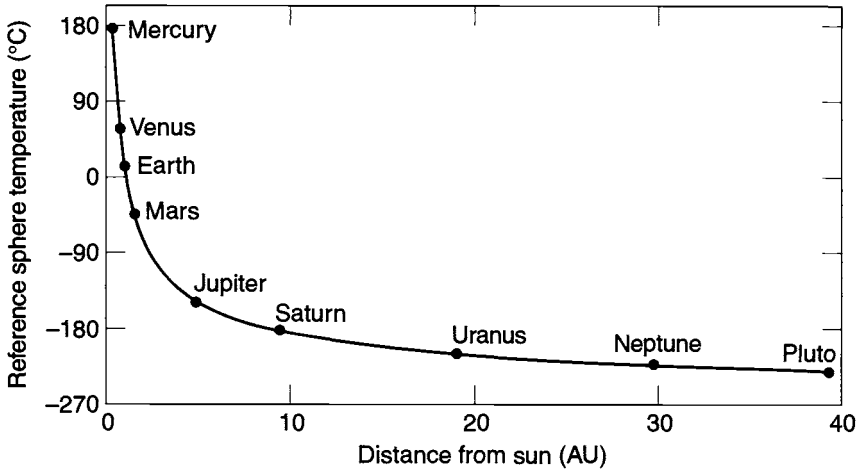


Fig. 2.26. Temperature as a function of distance from the sun.

temperature as a function of distance from the sun. At Earth's distance, the sphere's temperature is a relatively comfortable 6°C. At the average orbital distance of Mercury, the temperature is a scorching 174°C. At Mars, it falls to -47°C. For the outer planets, temperature drops sharply: -150°C for Jupiter, -183°C for Saturn, -209°C for Uranus, -222°C for Neptune, and -229°C for Pluto/Charon.

During planetary flybys, planet IR and albedo loads are added to the solar load for short periods of time. On most spacecraft, the thermal mass of the vehicle largely damps out the temperature rise of most components during flyby. Exposed lightweight components, however, may be significantly affected.

Environments of Mercury

Since Mercury is the closest planet to the sun, the thermal environment in its vicinity is, understandably, hot! Because Mercury's orbital period (its "year") is about 88 Earth days long and its period of rotation is approximately 58 Earth days, Mercury's "day" lasts for 176 Earth days. The rotation is so slow, in fact, that the surface temperature of the side of the planet facing the sun is essentially in equilibrium with the solar flux while the dark side is quite cold. Thus, the surface temperature, which drives the planetary IR emission, falls off as a cosine function from the subsolar region to the terminator. Mercury has no atmosphere to attenuate radiation from the surface to space. Hanson describes the surface temperature as a function of angle from the subsolar point as follows:^{2,21}

$$T = T_{\text{subsolar}}(\cos \phi)^{1/4} + T_{\text{terminator}}\left(\frac{\phi}{90}\right)^3 \quad \text{for } \phi \leq 90^\circ \quad (2.10)$$

$$T = T_{\text{terminator}} \quad \text{for } \phi > 90^\circ \quad (2.11)$$

where

$$T_{\text{subsolar}} = 407 \pm \frac{8}{r^{0.5}} \text{ K}, \tag{2.12}$$

$T_{\text{terminator}}$ is 110 K, ϕ is the angle from the subsolar point, and r is the Mercury-Sun distance in AUs.

The range of planetary emission corresponding to the above equations (see Table 2.6) is a remarkable 6 to 12,700 W/m²! (To avoid confusion and potential analysis errors, note that this surface-temperature model assumes a surface emittance of 0.77±0.06. Most other discussions of a planet’s effective surface temperature treat the surface as a blackbody with an emittance of 1.0. If the blackbody approach were used here, the calculated surface temperatures would be somewhat lower than what is shown above.)

The high surface temperatures on Mercury are driven by its proximity to the sun and generally low albedo. Depending on the geological features in the region being considered, specific albedo values can range from 0.08 to 0.25, as shown in Table 2.7 (from Murray *et al.*), meaning that most of the incident solar energy is absorbed and reradiated as planetary IR.^{2,22}

If the black reference sphere introduced earlier were placed in a circular orbit around Mercury at an altitude of 0.1 planet radii, its instantaneous temperature would range from 336 to -197°C, as shown in Table 2.8. The exceptionally wide swing in temperature (336 to -197°C) in the $\beta = 0^\circ$ orbit is a reflection of the eclipse plus the big difference between the surface temperatures, and therefore planetary IR, on the dayside and nightside. The orbit-average temperatures of 27

Table 2.6. Mercury Orbital Environments

	Perihelion	Aphelion	Mean
Direct solar (W/m ²)	14,462	6278	9126
Albedo (subsolar peak)	0.12	0.12	0.12
Planetary IR (W/m ²)			
Maximum (subsolar peak)	12,700	5500	8000
Minimum (dark side)	6	6	6

Table 2.7. Normal Albedo of Mercury

Geological Features	Albedo Values
Bright craters and rays	0.19 to 0.25
Heavily cratered terrain and textured plains	0.11 to 0.19
Flat-floored plains	0.10 to 0.13
Smooth plains	0.08 to 0.12

Table 2.8. Reference Sphere in Orbit Around Mercury

	$\beta = 0^\circ$		$\beta = 90^\circ$	
	Perihelion ($^\circ\text{C}$)	Aphelion ($^\circ\text{C}$)	Perihelion ($^\circ\text{C}$)	Aphelion ($^\circ\text{C}$)
Maximum	336	222	245	147
Minimum	-197	-197	245	147
Average	89	27	245	147

to 245°C are quite high, as one would expect to find at distances so close to the sun. The eccentricity of Mercury's orbit also results in unusually large differences between perihelion and aphelion solar flux and planetary IR, which are reflected in the significantly different temperatures of our reference sphere under perihelion and aphelion conditions.

Environments of Venus

The thermal environment in orbit around Venus is not only considerably cooler than the environment around Mercury because of Venus's greater distance from the sun, but it is also considerably different in terms of the relative contribution of the solar and IR components. The fact that Mercury's albedo is very low means that most of the incident solar energy is absorbed by the planet's surface, then reradiated as IR energy. Venus, on the other hand, is entirely covered by clouds and therefore has a very high albedo of around 0.8, as shown in Table 2.9. This high albedo results in a low cloud-top temperature and a planetary IR emission (Table 2.10, from Tomasko *et al.*) that is even less than that of Earth.^{2,23}

The cloud system of Venus also causes some solar backscattering effects at large angles from the subsolar point. These effects in turn create some limb-brightening near the terminator. For low-altitude orbits, modeling Venus's albedo as diffuse (Lambertian) with a cosine falloff from the subsolar point, as most analysis codes do, is fairly accurate. In fact, at the subsolar point, this approach is slightly conservative for altitudes up to about 1700 km (0.28 Venus radii). For higher altitudes, the limb-brightening effect becomes more prevalent, and consequently the assumption of diffuseness can underestimate albedo loads by about 10% for a spacecraft at an altitude of 6070 km (1 Venus radius) and by up to 41% at very large altitudes. However, because the albedo flux is fairly small at those altitudes, especially in comparison to the direct solar, this nonconservatism may not be particularly significant. Full evaluation of Venus's directional albedo characteristics is therefore recommended only for particularly sensitive components.

Table 2.9. Venus Orbital Environments

	Perihelion	Aphelion	Mean
Direct solar (W/m^2)	2759	2650	2614
Albedo	0.8 ± 0.02	0.8 ± 0.02	0.8 ± 0.02
Planetary IR (W/m^2)	153	153	153

Table 2.10. Planetary IR Emission of Venus

Latitude (deg)	Emission Flux (W/m^2)	T ($^{\circ}\text{C}$)
0–10	146.3	–47.6
10–20	153.4	–44.9
20–30	156.7	–43.7
30–40	158.7	–43.0
40–50	155.5	–44.2
50–60	152.0	–45.5
60–70	138.5	–50.7
70–80	143.5	–48.7
80–90	178.4	–36.2

Placing our black reference sphere in a 607-km-altitude (0.1-radii-altitude) orbit around Venus produces the temperatures shown in Table 2.11. Although Venus is generally much cooler than Mercury, it does share with that planet a large temperature swing in the $\beta = 0^{\circ}$ orbit. In the case of Mercury, the swing is driven by large planetary IR loads from the sunlit side of the planet. For Venus, the high temperatures are caused by the very large albedo loads. Temperatures during the eclipsed portion of the orbit are somewhat higher than is the case for Mercury, as a result of Venus's higher planetary IR on the dark side. Venus's orbit, like those of most of the planets, does not have as high an eccentricity as Mercury's, so the temperatures of the reference sphere are not greatly different for perihelion and aphelion conditions.

Lunar Environments

As a result of the lack of an atmosphere and the length of the lunar day, the thermal environment in orbit around the moon is similar to that around Mercury; it is dominated by planetary IR that diminishes as a cosine function of the angle from the subsolar point. The moon's equatorial surface-temperature distribution, which drives the emitted IR, is shown versus angle from the subsolar point in Fig. 2.27. It is derived from Apollo 11 data (by Cremers, Birkebak, and White) using a cosine

Table 2.11. Reference Sphere in Orbit Around Venus

	$\beta = 0^{\circ}$		$\beta = 90^{\circ}$	
	Perihelion ($^{\circ}\text{C}$)	Aphelion ($^{\circ}\text{C}$)	Perihelion ($^{\circ}\text{C}$)	Aphelion ($^{\circ}\text{C}$)
Maximum	122	119	67	64
Minimum	–105	–105	67	64
Average	14	12	67	64

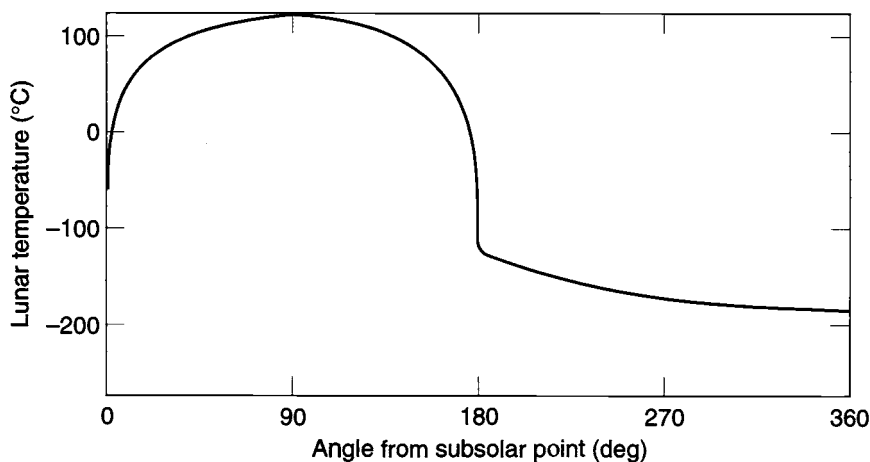


Fig. 2.27. Lunar surface temperature.

relationship for temperature to about 70 deg and assumes a surface emittance of 0.92.^{2,24} A similar distribution is thought to apply in all directions from the subsolar point, not just in the equatorial plane. The temperature on the dark side of the moon is on the order of -170°C .

As bright as the moon may appear in the night sky, its average albedo is only 0.073, making it as absorptive as black paint! Even the most reflective lunar geological regions have albedo values less than 0.13, as shown in Table 2.12 (from Ref. 2.25). This low albedo (high absorptance) causes the high surface temperature on the sunlit side. A summary of the moon's thermal environmental parameters is shown in Table 2.13.

When our reference sphere is placed in orbit around the moon at an altitude of 0.1 lunar radii, we see a temperature response (Table 2.14) qualitatively like the response of Mercury, with high temperatures over the subsolar point and very low temperatures during eclipse. This pattern, again, is characteristic of the long day

Table 2.12. Albedo of Lunar Surface Features

Geological Regions	Normal Albedo ^a
Copernican-type craters	0.126
Apennine Mountains	0.123
Mare Serenitatis	0.093
Mare Tranquillitatis	0.092
Mare Fecunditatis	0.092
Langrenus Crater	0.129

^aApproximate average values.

Table 2.13. Lunar Orbital Environments

	Perihelion	Aphelion	Mean
Direct solar (W/m^2)	1414 ± 7	1323 ± 7	1368 ± 7
Albedo (subsolar peak)	0.073	0.073	0.073
Planetary IR			
Maximum (W/m^2) (subsolar peak)	1314	1226	1268
Minimum (W/m^2) (dark side)	5.2	5.2	5.2

Table 2.14. Reference Sphere in Orbit Around the Moon

	$\beta = 0^\circ$		$\beta = 90^\circ$	
	Perihelion ($^\circ C$)	Aphelion ($^\circ C$)	Perihelion ($^\circ C$)	Aphelion ($^\circ C$)
Maximum	67	61	22	17
Minimum	-199	-199	22	17
Average	-56	-59	22	17

and the lack of an atmosphere to retain surface heat; these factors combine to produce very low dark-side surface temperatures and, consequently, minimal dark-side planetary IR.

The Apollo program missions have provided interesting lessons pertaining to spacecraft thermal balance, both in orbit around the moon and on its surface. The planetary IR is so large in lunar orbit that spacecraft radiator surfaces are affected to a much greater extent than they are in Earth orbit. In particular, the lesson here is to choose radiator locations and spacecraft attitude to minimize radiator views to the lunar surface, when possible. Since most radiators have a low solar absorptance and high IR emittance, pointing the radiator towards the sun to some extent, to minimize its view to the lunar surface, is frequently preferable.

A similar effect has occurred during lunar surface operations of Apollo missions. The proximity of relatively low mountains near Hadley Rille (Apollo 15) and Taurus Littrow (Apollo 17) affected the thermal performance of lunar surface equipment. Specifically, electronic equipment with zenith-pointing radiators actually had small view factors (a few percent) to the nearby mountains. The IR load from the hot mountains raised temperatures of the equipment by at least $10^\circ C$. Thus, the presence of mountains for lunar surface operations cannot be ignored.

Another important factor in lunar surface operations is dust, which can easily be thrown up by lunar rover operations or just by a person walking. Since lunar dust is very dark, a small amount settling on radiators can significantly raise their normally low solar absorptance. This effect was so strong that, by the last Apollo Lunar Rover mission, the crew brushed dust off radiator surfaces at almost every stop of the Rover vehicle.

The last lesson to note is the effect of the extremely low thermal conductivity of lunar soil. The low conductivity results in the surface temperature in shadowed areas almost reaching the -170°C nightside value very quickly. These shadowed “cold spots” in the proximity of surface equipment can substantially reduce the IR load on the equipment. These were of particular concern for the operators of the Apollo 14 Modular Equipment Transporter, which had rubber tires whose lower temperature limit was -57°C . The shadows created by the tires themselves required that the vehicle be parked such that one tire did not shadow the other, creating a tire undertemperature condition.

Environments of Mars

Mars is the last planet in our tour of the solar system near which a spacecraft will experience significant environmental heating. The average solar flux (see Table 2.15) is 589 W/m^2 , or about 42% of what is experienced by an Earth-orbiting spacecraft. As a result of the eccentricity of Mars’s orbit, however, the solar flux at Mars varies by $\pm 19\%$ over the Martian year, which is considerably more than the $\pm 3.5\%$ variation at Earth. Albedo fractions are similar to Earth’s, being around 0.25 to 0.28 at the equator and generally increasing toward the poles, as shown in Table 2.16. Like Earth’s poles, the reflective polar caps of Mars are responsible for the planet’s high albedo at high latitudes. Befitting the “red planet,” the spectral distribution of Martian albedo, compared to other planets’ albedos, shows a shift to the red end of the spectrum, peaking at $0.7\ \mu\text{m}$ (Earth albedo peaks at $0.47\ \mu\text{m}$).

Martian planetary IR values have been derived from Mariner and Viking Orbiter spacecraft data. The best description is a plot of equivalent blackbody (emittance = 1.0) surface temperature vs. latitude and longitude for both perihelion and aphelion conditions, as shown in Figs. 2.28 and 2.29. These data, derived from Palluccone and Kieffer,^{2,26} are currently used in the design of Mars-orbiting spacecraft.

The data are based on an assumption that the environments described above experience no dust storms. The presence of a global dust storm would slightly increase the overall albedo, with dark-area albedos increasing more than bright-area ones. The increased atmospheric opacity would also damp the effective diurnal temperature range, making the planetary IR more benign.

Our reference sphere, in orbit around Mars at a 0.1-planet-radius altitude, experiences instantaneous temperatures from $+11$ to -163°C and orbit averages from -22 to -82°C , as shown in Table 2.17. Mars’s thin, relatively cloudless atmosphere

Table 2.15. Mars Orbital Environments

	Perihelion	Aphelion	Mean
Direct solar (W/m^2)	717	493	589
Albedo (subsolar peak)	0.29	0.29	0.29
Planetary IR			
Maximum (W/m^2) (near subsolar)	470	315	390
Minimum (W/m^2) (polar caps)	30	30	30

Table 2.16. Mars Albedo Distribution

Latitude (deg)	Maximum Albedo	Minimum Albedo
80 to 90	0.5	0.3
70 to 80	0.5	0.2
60 to 70	0.5	0.2
50 to 60	0.5	0.17
40 to 50	0.28	0.17
30 to 40	0.28	0.18
20 to 30	0.28	0.22
10 to 20	0.28	0.25
0 to 10	0.28	0.25
-10 to 0	0.28	0.20
-20 to -10	0.25	0.18
-30 to -20	0.22	0.18
-40 to -30	0.22	0.18
-50 to -40	0.25	0.3
-60 to -50	0.25	0.4
-70 to -60	0.3	0.4
-80 to -70	0.4	0.4
-90 to -80	0.4	0.4

Table 2.17. Reference Sphere in Orbit Around Mars

	$\beta = 0^\circ$		$\beta = 90^\circ$	
	Perihelion (°C)	Aphelion (°C)	Perihelion (°C)	Aphelion (°C)
Maximum	11	-16	0	-26
Minimum	-162	-163	-32	-53
Average	-63	-82	-22	-43

is highly transmissive to IR. This condition contributes to the cold nighttime surface temperatures and causes nightside planetary IR to be much lower than that on the dayside. The low temperature of our sphere during the $\beta = 0^\circ$ eclipse is a consequence of this surface cooling. This variation contrasts with the more uniform planetary IR of Earth and Venus, both of which have atmospheres that impede radiation from the surface to space, giving those planets more uniform day and night temperatures.

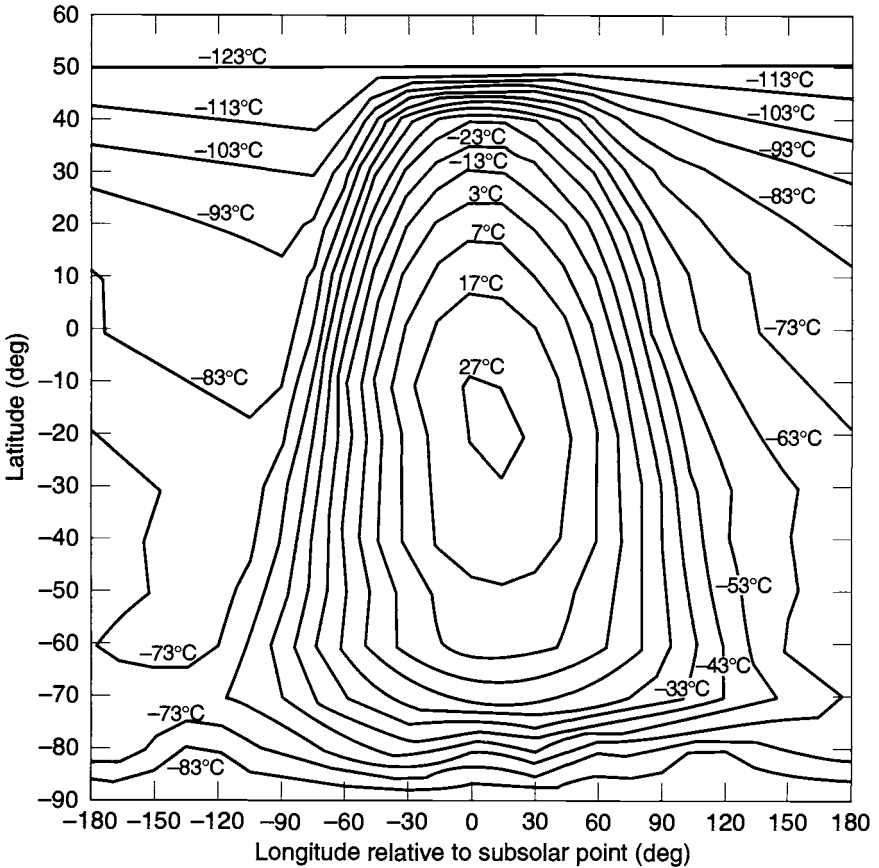


Fig. 2.28. Mars perihelion surface temperature.

Environments of the Outer Planets

The thermal environments of the outer planets, Jupiter through Pluto/Charon (Refs. 2.27 through 2.32), are very cold as a result of their large distances from the sun. Solar intensity drops by more than an order of magnitude between Mars and Jupiter. Substances that are gases on Earth become liquids and solids on these extremely cold worlds. Solar, albedo, and planetary IR fluxes in the vicinity of these planets are small compared to the IR emitted by room-temperature objects. Under these conditions, environmental loads can often be ignored in the thermal

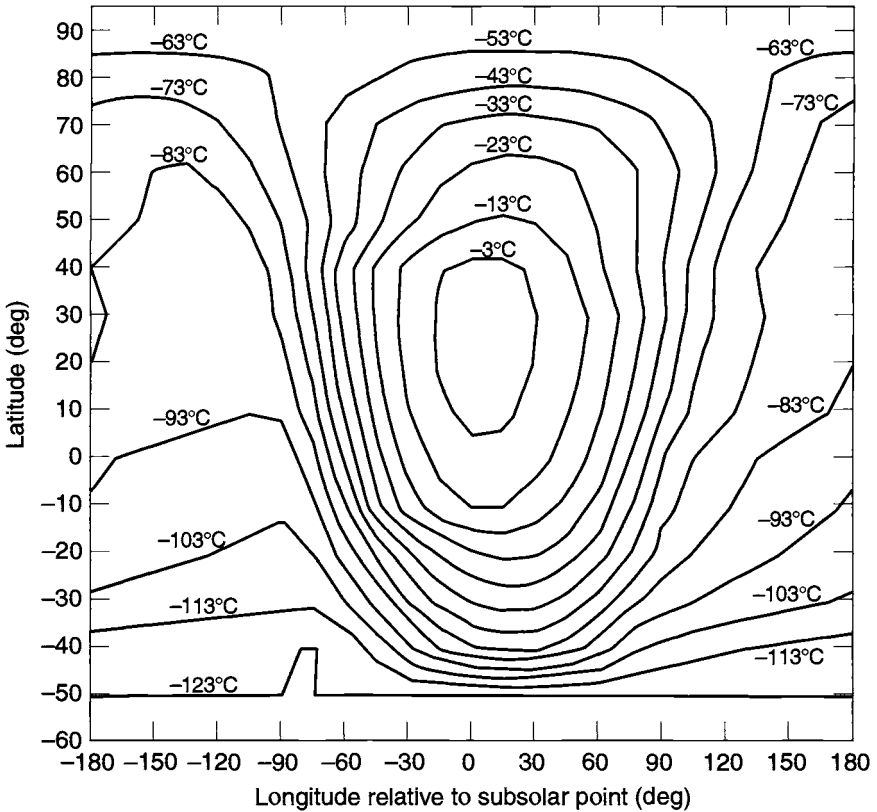


Fig. 2.29. Mars aphelion surface temperature.

design and analysis of spacecraft hardware that functions at room temperature, such as payload electronics. Only sensitive instruments, cryogenic radiators, and exposed, uninsulated components will register the feeble effects of environmental heat loads in the vicinity of these planets.

Table 2.18 summarizes the environmental parameters of the outer planets and identifies associated references. The temperature of our reference sphere in orbit around each planet is shown in Table 2.19. As these numbers indicate, thermal control of spacecraft in this part of the solar system is about keeping things warm. There is no "hot" environment!

Table 2.18. Outer-Planet Orbital Environments

Planet	Perihelion	Aphelion	Mean	Reference
Jupiter				
Direct solar (W/m ²)	56	46	51	
Albedo	0.343	0.343	0.343	24
Planetary IR (W/m ²)	13.7	13.4	13.6	24
Saturn				
Direct solar (W/m ²)	16.8	13.6	15.1	
Albedo	0.342	0.342	0.342	25
Planetary IR (W/m ²)	4.7	4.5	4.6	25
Uranus				
Direct solar (W/m ²)	4.09	3.39	3.71	
Albedo	0.343	0.343	0.343	26
Planetary IR (W/m ²)	0.72	0.55	0.63	27
Neptune				
Direct solar (W/m ²)	1.54	1.49	1.51	
Albedo	0.282	0.282	0.282	26
Planetary IR (W/m ²)	0.52	0.52	0.52	28
Pluto/Charon				
Direct solar (W/m ²)	1.56	0.56	0.88	
Albedo	0.47	0.47	0.47	29
Planetary IR (W/m ²)	0.8	0.3	0.5	29

Aerobraking Environments

Aerobraking maneuvers, as mentioned in Chapter 1, are sometimes used to make large changes in orbit altitude or inclination, and they are especially useful in slowing down a spacecraft on an interplanetary trajectory to the point where orbital capture by a planet is possible. Aerobraking occurs when a portion of the orbit enters a planet's atmosphere, creating aerodynamic drag on the spacecraft (Fig. 2.30). This drag slows the spacecraft, thereby gradually lowering the altitude or changing the orbital plane, and it can also rapidly warm the spacecraft because of friction in the atmosphere. The advantage aerobraking provides is placement

Table 2.19. Reference Sphere in Orbit Around the Outer Planets

	$\beta = 0^\circ$		$\beta = 90^\circ$	
	Perihelion ($^\circ\text{C}$)	Aphelion ($^\circ\text{C}$)	Perihelion ($^\circ\text{C}$)	Aphelion ($^\circ\text{C}$)
Jupiter				
Maximum	-130	-136	-139	-144
Minimum	-181	-182	-139	-144
Average	-154	-57	-139	-144
Saturn				
Maximum	-167	-171	-173	-177
Minimum	-203	-203	-173	-177
Average	-183	-186	-173	-177
Uranus				
Maximum	-200	-203	-204	-208
Minimum	-229	-232	-204	-208
Average	-213	-216	-204	-208
Neptune				
Maximum	-214	-215	-217	-218
Minimum	-232	-232	-217	-218
Average	-223	-223	-217	-218
Pluto/Charon				
Maximum	-211	-225	-215	-228
Minimum	-228	-238	-215	-228
Average	-219	-231	-215	-228

of the spacecraft into the desired orbit at reduced mass and cost. Without an aerobraking maneuver, a spacecraft would require additional fuel, and possibly additional thrusters, to adjust the orbit or achieve planetary orbit capture.

The heating rates that the spacecraft will be exposed to during an aerobraking maneuver are usually calculated by specialists in orbit dynamics and atmospheric sciences and are provided to the thermal engineer as a heating rate per unit area normal to the spacecraft velocity vector. Several parameters must be considered, however, to fully characterize the thermal effects of aerobraking on the spacecraft.

The duration and intensity of the aeroheating need to be identified for each successive pass through the atmosphere, with the effects of any potential navigation errors (e.g., velocity or altitude) conservatively included. Because aerobraking orbits decay primarily by decreases in the apogee, more severe orbit-average heating

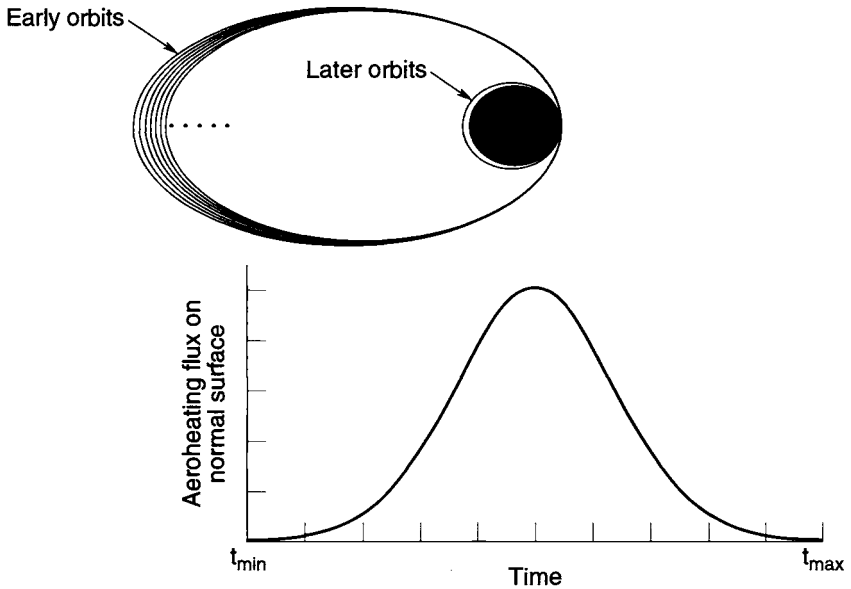


Fig. 2.30. Representative aerobraking maneuver and heating rates.

can result over successive orbits because the fraction of time during which aeroheating occurs increases as the orbit period decreases. Finally, the thermal engineer must analytically determine the heating rate for each spacecraft surface by multiplying the heating rate provided by the orbit analysts by the cosine of the angle between the velocity vector and the surface. The thermal analyst must then use the calculated heating rates to assess the impact of aeroheating on the entire spacecraft with a conservative, detailed transient analysis of the aerobraking maneuver.

Along with the mass advantages of aerobraking to the mission come numerous challenges to the thermal design. Aerobraking maneuvers can be the stressing hot-case condition that drives the design of some spacecraft components. Frequently, orbit analysts want to increase aerodynamic drag by positioning large deployable appendages, such as solar arrays, so that their surface area normal to the spacecraft velocity vector is maximized. Unfortunately, such positioning results in maximum aeroheating as well. Therefore, spacecraft attitude and configuration compromises to mitigate the thermal impact of the aerobraking maneuver are common. Deployables, often with a low thermal mass per unit area, should receive special attention from the thermal analysis to ensure temperature requirements are not exceeded. Also, if the spacecraft orientation vector has a known uncertainty, the thermal engineer should examine several possible orientation angles to make sure that the most severe aeroheating for each sensitive component is identified.

One component of most thermal designs that is vulnerable to aeroheating is the multilayer insulation (MLI) blanket. Since MLI is naturally insulating and the

outer layers possess a very low thermal mass per unit area, a blanket exposed to significant aeroheating will reach very high temperatures (possibly exceeding 300°C) in a negligible amount of time. Typical MLI materials, such as Mylar interior layers and Dacron scrim, may not survive the severity of the aerobraking maneuver. Alternate high-temperature MLI designs, such as those discussed in Chapter 5, can survive much higher temperatures and should provide adequate radiative insulation.

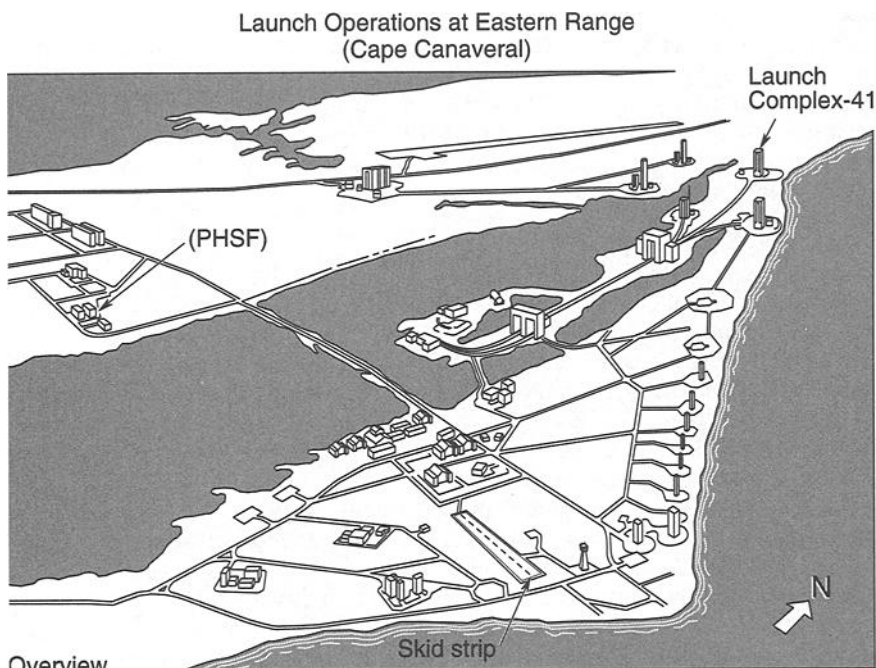
Launch and Ascent Environments

Spacecraft thermal-control systems are usually designed to the environment encountered on orbit. Vehicle temperatures during transportation, prelaunch, launch, and ascent must be predicted, however, to ensure temperature limits will not be exceeded during these initial phases of the mission. In some cases, thermal design changes or constraints on launch environments, such as maximum eclipse duration or FMH rates, are necessary to prevent excessively high or low temperatures from occurring on the spacecraft.

The transportation and prelaunch phases usually include shipping of the spacecraft, preparations and testing in the clean room at the launch site, and the final countdown period with the spacecraft on the booster at the launchpad. A typical transportation sequence is shown in Fig. 2.31. Thermal control during these phases is generally achieved by controlling the environment. For transportation, when the spacecraft is not powered, ambient temperature and humidity limits are specified to keep all components within nonoperating temperature limits and to prevent moisture condensation. During testing and storage at the launch site, room temperature conditions may be acceptable, or constraints may be required on how long the vehicle may be powered up to prevent reaching operating-temperature limits. If these “passive” approaches are not sufficient, special air-conditioning units may be required to blow cold air into or onto the spacecraft when it is powered on, although this is unusual.

Once the spacecraft is encapsulated in the booster fairing or placed in the space-shuttle cargo bay on the pad, thermal control is achieved by blowing conditioned air or nitrogen through the fairing enclosure. The inlet temperature of this conditioned gas is usually specifiable over some nominal range such as 10–27°C for the Titan IV or 7–32°C for the shuttle. The temperature of the gas may warm or cool significantly from heat gained or lost to the payload fairing or shuttle vehicle as the gas flows through the payload compartment. The electronic waste heat generated by most spacecraft, however, is usually not sufficient to cause a significant rise in purge-gas temperature.

With some spacecraft, thermal analysis of prelaunch conditions may show that purge gas alone may not be enough to provide adequate cooling for all components. If this is the case, special air- or liquid-cooling ducts or loops may be required to provide extra cooling. However, since these cooling loops add significant cost and complexity to launch thermal control and may sometimes present reliability problems, the engineer should investigate other options, such as intermittently turning off components, before implementing special cooling provisions.



- C5-A arrives at skid strip
- Satellite shipping container convoys to Payload Hazardous Safe Facility (PHSF)
- Satellite processed to vertical in PHSF and convoys to LC-41
- Hoist satellite at LC-41 and mate to booster

Fig. 2.31. Launch site processing.

From liftoff through final orbit insertion, the thermal environment becomes more severe. The approach is to predict spacecraft temperatures for the worst hot and cold conditions and, where necessary, implement constraints on such values as maximum eclipse time and maximum FMH. Changes to the thermal design or severe constraints on launch are usually implemented only as a last resort.

A typical launch-and-ascent sequence for an expendable booster is shown in Fig. 2.32. For the first few minutes the environment surrounding the spacecraft is driven by the payload-fairing temperature, which rises rapidly to 90–200°C as a result of aerodynamic heating. Fairing temperatures for the Atlas II booster are shown in Fig. 2.33. During the same period, a very slight cooling effect results from the depressurization of the gas in the payload compartment. This cooling effect, however, is very feeble; it is noticeable for only a few minutes on very low-mass items such as the outer layer of an MLI blanket, and it is usually ignored in launch thermal analysis. The effects of the payload-fairing temperature rise are more significant, but they will still only cause a temperature rise on relatively low-mass, exposed components such as solar arrays, insulation blankets, antennas, and very lightweight structures. The effect is further mitigated on some boosters by acoustic blankets inside the fairing that also provide an insulating effect.

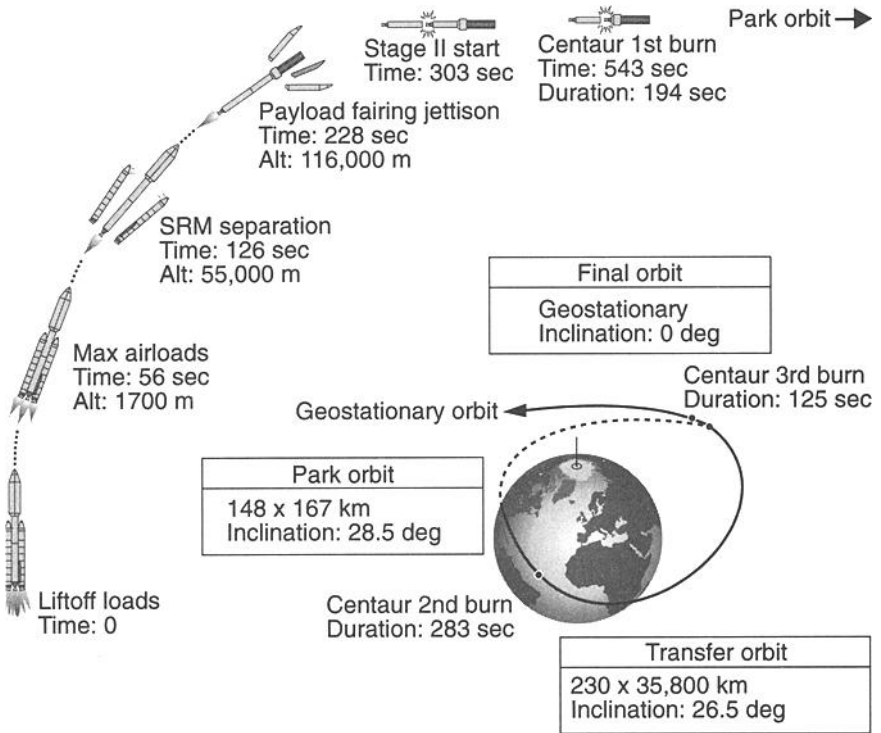


Fig. 2.32. Representative geosynchronous mission profile.

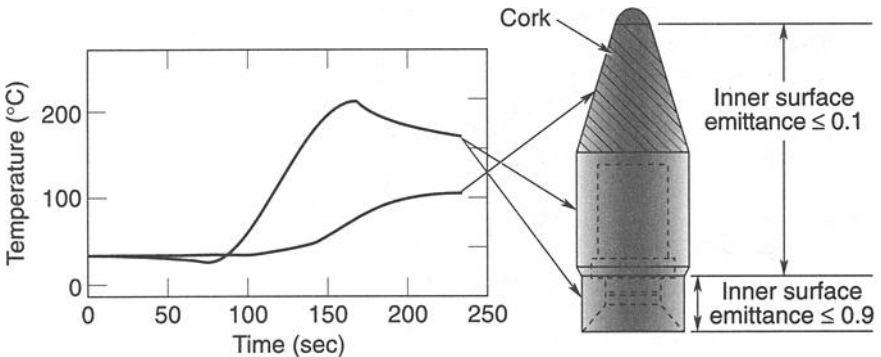


Fig. 2.33. Atlas fairing temperatures.

Within 2 to 5 min after liftoff, the vehicle is high enough that aerodynamic effects are gone and FMH drops low enough that the fairing may be jettisoned to save weight and thereby increase payload capacity. Because dropping the fairing

as soon as possible is desirable, FMH rates are usually still very significant for up to 30 min after fairing separation. Curves of FMH versus time are usually generated by the booster contractor using sophisticated atmospheric and trajectory simulation codes, and they are supplied to the spacecraft thermal engineers. These curves may be complex, rising and falling as the booster altitude and velocity change, as shown in the sample curve of Fig. 2.6.

From the time of fairing separation onward, the spacecraft is exposed to a combination of FMH, solar, Earth IR, and albedo loads, and sometimes plume heating effects from the main rocket engines and attitude-control thrusters. During rocket firing, the attitude is set by guidance considerations. Between burns, however, the attitude may be changed for thermal or other reasons. It is not uncommon for the upper stage/spacecraft to go into a "barbecue roll" during these coast periods to maintain a moderate thermal environment for the payload. A thermal analysis is required to verify that spacecraft temperatures remain within limits under the combination of conditions discussed above. If temperature limits are exceeded, constraints on FMH, eclipse time, vehicle attitudes, or prelaunch purge temperatures are negotiated with the booster contractor to moderate the thermal environment. If such constraints are impractical, thermal design changes may be required to resolve the problem.

The ascent phase typically lasts 30 to 45 min and results in insertion either into a temporary parking orbit, into a transfer orbit, or directly into the final mission orbit. Direct insertion into the final orbit may occur for low Earth or highly elliptical (e.g., Molniya) orbits. Higher-altitude circular orbits, such as GEO or 12-hour orbits, require an elliptical transfer orbit to move the spacecraft to the higher altitude. An apogee-kick-motor burn at the apogee of the transfer orbit makes the orbit circular at the desired altitude (see Fig. 2.32). During the parking or transfer orbits, the spacecraft will be exposed to the usual solar, IR, and albedo loads and is usually in a reduced power mode with appendages such as solar arrays stowed. Eclipses during transfer orbits to GEO altitudes can last as long as 3.5 hours. This is almost three times longer than the maximum eclipse in GEO orbits and can present thermal-control problems if eclipse times are not limited by launch constraints. Because of the reduced power dissipation and long eclipses, the most common concern during this period is unacceptably low temperatures on the spacecraft, although high temperatures can occur if the spacecraft is inertially stable with the sun shining continuously on a sensitive component.

Once the spacecraft reaches its final orbit, a period lasting anywhere from a few hours to several weeks occurs, during which the spacecraft attitude is stabilized, appendages such as solar arrays and antennas are deployed, and bus and payload electronics are powered up. The thermal-control system must maintain acceptable temperatures during this period, and survival heaters are sometimes required. The sequence of events—when certain attitudes are achieved, when payloads are turned on, and so on—is also sometimes driven by thermal considerations.

For launches on the space shuttle, the prelaunch, ascent, and transfer-orbit events are similar to those of the expendable booster. The shuttle, however, has a far more complex park-orbit condition during which the spacecraft may be exposed to a wide range of thermal conditions for periods ranging from six hours

to several days, with the longer duration typically a result of contingency operations or multiple payload deployments. Unlike an expendable booster, which jettisons its fairing a few minutes after liftoff, the shuttle doors may remain closed for up to three hours, limiting the payload spacecraft's ability to reject waste heat. Once the doors are open, the bay may be pointed toward Earth, which is fairly benign, or toward deep space or the sun, in which case the environments are more severe. Maneuvers are also required periodically for shuttle guidance-system alignments, communication, etc. Because the bay liner is insulated, a spacecraft sitting in the shuttle payload bay may be exposed to more extreme conditions than if it were on a conventional booster, where it would simultaneously see a combination of sun, Earth, and deep space. In addition to the complex on-orbit environment, abort reentry conditions must also be considered. This additional complexity, along with safety considerations, makes the thermal integration process an order of magnitude more difficult for a shuttle launch than for a launch on a conventional booster.

A more in-depth discussion of spacecraft-to-launch-vehicle thermal integration is contained in Refs. 2.33 and 2.34, which cover integration with the Titan IV and space-shuttle launch vehicles, respectively, and Chapter 18, which discusses the shuttle integration process in detail.

References

- 2.1. C. Fröhlich and R. W. Brusa, "Solar Radiation and Its Variation in Time," *Sol. Phys.* **74**, 209–215 (1981).
- 2.2. C. Fröhlich and C. Wehrli, "Spectral Distribution of Solar Irradiance from 25000 nm to 250 nm," World Radiation Center, Davos, Switzerland, 1981.
- 2.3. "Solar Electromagnetic Radiation," NASA SP-8005 (May 1971).
- 2.4. "Earth Albedo and Emitted Radiation," NASA SP-8067 (July 1971).
- 2.5. D. F. Gluck, "Space Vehicle Thermal Testing: Environments, Related Design and Analysis, Requirements, and Practice," The Aerospace Corporation, Report No. TOR-86A(2902-08)-1, 27 September 1987.
- 2.6. G. L. Stephens, G. G. Campbell, and T. H. Von der Haar, "Earth Radiation Budgets," *J. Geophys. Res.* **86** (20 October 1981).
- 2.7. G. L. Smith, D. Rutan, and T. D. Bess, "Atlas of Albedo and Absorbed Solar Radiation Derived from Nimbus 7 Earth Radiation Budget Data Set—November 1978 to October 1985," NASA Ref. Pub. 1231, 1990.
- 2.8. R. L. Collins, "Albedo and Earthshine," The Aerospace Corporation IOC 87.5462.4-25, 27 April 1987.
- 2.9. M. Donabedian, "Thermal Uncertainty Margins for Cryogenic Sensor Systems," The Aerospace Corporation, ATM 90(9975)-3, 21 November 1989.
- 2.10. D. S. Glaister, "Space Environment for Cryogenic Radiator," The Aerospace Corporation, ATM No. 90(9975)-35, 3 May 1990.
- 2.11. B. R. Barkstrom and G. L. Smith, "The Earth Radiation Budget Experiment: Science and Implementation," *Rev. Geophys.* **24**, 379–390 (1986).

- 2.12. B. R. Barkstrom, E. Harrison, G. Smith, R. Green, J. Kibler, R. Cess, and ERBE Science Team, "Earth Radiation Budget Experiment (ERBE Archival and April 1985 Results)." *Bull. Am. Meteorol. Soc.* **70** (10), 1254–1262 (1989).
- 2.13. T. D. Bess and G. L. Smith, "Earth Radiation Budget: Results of Outgoing Long-wave Radiation from Nimbus-7, NOAA-9, and ERBS Satellites," *J. Appl. Meteorol.* **32** (5), 813–824 (1993).
- 2.14. "Natural Orbital Environment Criteria Guidelines for Use in Space Vehicle Development," NASA Technical Memorandum 4527, June 1994.
- 2.15. B. J. Anderson, C. G. Justus, and W. Batts, "Guidelines for the Selection of Near-Earth Thermal Environment Parameters for Spacecraft Design," NASA Technical Memorandum TM-2001-211221 (October 2001).
- 2.16. C. Y. Fan *et al.*, "Dynamics and Structure of the Outer Radiation Belt," *J. Geophys. Res.* **66**, 2207 (1961).
- 2.17. B. J. O'Brian. *et al.*, "Absolute Electron Intensities in the Heart of the Earth's Outer Radiation Zone," *J. Geophys. Res.* **67**, 1 (1962).
- 2.18. A. J. Dessler and R. Karplus, "Some Properties of the Van Allen Radiation," *Phys. Rev. Letters* **4**, 271 (1960).
- 2.19. J. I. Vette, Models of the Trapped Radiation Environment, Vol. I and II, NASA Rept. SP-3024 (1966).
- 2.20. R. D. Jimenez, "Natural Environment Charged Particle Heating of Spacecraft Cryogenic Components," The Aerospace Corporation, Report No. TOR-0088(3062)-3, 19 September 1988.
- 2.21. O. L. Hanson, "Surface Temperature and Emissivity of Mercury," *Astrophys. J.* **190**, 715–717 (15 June 1974).
- 2.22. B. C. Murray *et al.*, "Mercury's Surface: Preliminary Description and Interpretation from Mariner 10 Pictures," *Science* **185** (4146), 164–179 (12 July 1974).
- 2.23. M. G. Tomasko *et al.*, "The Thermal Balance of Venus in Light of the Pioneer Venus Mission," *J. Geophys. Res.* **85** (A13), 8187–8199 (30 December 1980).
- 2.24. C. J. Cremers, R. C. Birkebak, and J. E. White, "Lunar Surface Temperature at Tranquility Base," AIAA paper 71-79, *AIAA 9th Aerospace Sciences Meeting* (New York, New York, 1971).
- 2.25. Apollo 15 Preliminary Science Report NASA SP-289, 1972.
- 2.26. F. D. Pallucone and H. H. Kieffer, "Thermal Inertia Mapping of Mars from 60°S to 60°N," *Icarus* **45**, 415–426 (1981).
- 2.27. R. A. Hanel *et al.*, "Albedo, Internal Heat, and Energy Balance of Jupiter: Preliminary Results of the Voyager Infrared Investigation," *J. Geophys. Res.* **86** (A10), 8705–8712 (30 September 1981).
- 2.28. R. A. Hanel *et al.*, "Albedo, Internal Heat Flux, and Energy Balance of Saturn," *Icarus* **53**, 262–285 (1983).
- 2.29. J. B. Pollack *et al.*, "Estimates of the Bolometric Albedos and Radiation Balance of Uranus and Neptune," *Icarus* **65**, 442–466.
- 2.30. G. S. Orton, "Thermal Spectrum of Uranus: Implications for Large Helium Abundance," *Science* **231**, 836–840 (February 1986).
- 2.31. Preliminary Science Data from Voyager 2 Neptune Encounter, 25 August 1989.

- 2.32. S. R. Sawyer *et al.*, "Spectrophotometry of Pluto-Charon Mutual Events: Individual Spectra of Pluto and Charon," *Science* **238**, 1560–1563 (December 1987).
- 2.33. R. Pleasant and W. Kelly, "Thermal Integration of Satellite Vehicles with Titan/Centaur," AIAA 89-1723, *AIAA 24th Thermophysics Conference* (12–14 June, 1989).
- 2.34. "Shuttle/Payload Integration, Information Document for Thermal," NASA JSC-21000-INF, September 1986.